

Size-Selective Transfer of Lipid Nanoparticle-Based Drug Carriers Across the Blood Brain Barrier Via Vascular Occlusions Following Traumatic Brain Injury

Igor Khalin,* Nagappanpillai Adarsh, Martina Schifferer, Antonia Wehn, Bernhard Groschup, Thomas Misgeld, Andrey Klymchenko,* and Nikolaus Plesnila*

The current lack of understanding about how nanocarriers cross the blood-brain barrier (BBB) in the healthy and injured brain is hindering the clinical translation of nanoscale brain-targeted drug-delivery systems. Here, the bio-distribution of lipid nano-emulsion droplets (LNDs) of two sizes (30 and 80 nm) in the mouse brain after traumatic brain injury (TBI) is investigated. The highly fluorescent LNDs are prepared by loading them with octadecyl rhodamine B and a bulky hydrophobic counter-ion, tetraphenylborate. Using in vivo two-photon and confocal imaging, the circulation kinetics and bio-distribution of LNDs in the healthy and injured mouse brain are studied. It is found that after TBI, LNDs of both sizes accumulate at vascular occlusions, where specifically 30 nm LNDs extravasate into the brain parenchyma and reach neurons. The vascular occlusions are not associated with bleedings, but instead are surrounded by processes of activated microglia, suggesting a specific opening of the BBB. Finally, correlative light-electron microscopy reveals 30 nm LNDs in endothelial vesicles, while 80 nm particles remain in the vessel lumen, indicating size-selective vesicular transport across the BBB via vascular occlusions. The data suggest that microvascular occlusions serve as “gates” for the transport of nanocarriers across the BBB.

which result in severe cognitive, motor, and neuropsychiatric sequelae.^[1] Moreover, TBI increases the risk of neurodegenerative diseases, such as Alzheimer's or Parkinson's disease.^[2] To date, all clinical trials aimed to establish new pharmacological treatment for TBI have failed and thus no efficient therapeutic options exist to protect the brain from additional damage following a traumatic event.^[3]

A major hurdle for the development of novel pharmacotherapies for the treatment of central nervous system (CNS) disorders, including TBI, is the blood-brain barrier (BBB). The BBB bars many drugs from entering and accumulating in the brain parenchyma, therefore, BBB-permeable drug formulations often have to be applied in such high concentrations that the risk for adverse reactions is disproportionately elevated.^[4,5] Therefore, there is an urgent need for the development of drug delivery systems that trans-

port therapeutic molecules across the BBB and help to treat brain injuries.

Many studies have shown the accumulation of nanoscale drug carriers in the CNS after TBI^[6,7] or the central effects of their cargoes.^[8,9] For instance, we have previously demonstrated

1. Introduction

Traumatic brain injury (TBI) is the number one cause of death in young adults and children and is characterized by acute and chronic neuroinflammation and axonal degeneration

I. Khalin, A. Wehn, B. Groschup, N. Plesnila
Institute for Stroke and Dementia Research
University of Munich Medical Center
81377 Munich, Germany
E-mail: igor.khalin@med.uni-muenchen.de;
nikolaus.plesnila@med.uni-muenchen.de

I. Khalin, M. Schifferer, T. Misgeld, N. Plesnila
Cluster for Systems Neurology
Munich, Germany

 The ORCID identification number(s) for the author(s) of this article can be found under <https://doi.org/10.1002/smll.202200302>.

© 2022 The Authors. Small published by Wiley-VCH GmbH. This is an open access article under the terms of the Creative Commons Attribution License, which permits use, distribution and reproduction in any medium, provided the original work is properly cited.

DOI: 10.1002/smll.202200302

N. Adarsh, A. Klymchenko
Laboratory de Biophotonique et Pharmacologie
University of Strasbourg
Strasbourg 67401, France
E-mail: andrey.klymchenko@unistra.fr

N. Adarsh
Department of Polymer Chemistry
Government College Attingal
Kerala 695101, India

M. Schifferer, T. Misgeld
German Center for Neurodegenerative Diseases
81377 Munich, Germany

T. Misgeld
Institute of Neuronal Cell Biology
School of Medicine
Technical University of Munich
80802 Munich, Germany

that brain-derived neurotrophic factors delivered by polymeric nanoparticles (NPs) accumulated in the injured mouse brain and improved neurological outcomes.^[10] Using real-time two-photon microscopy, we demonstrated the accumulation of ultrabright NPs in the brain after brain injury.^[11] However, it still remains unclear how NPs are transported from the blood stream into the brain parenchyma – where this transport occurs – and which cellular elements are involved.^[12] Attempts to answer these questions were made by using magnetic resonance imaging and conventional fluorescence microscopy.^[6,13] However, these approaches are so limited in the resolution that many questions regarding the spatio-temporal dynamics of NPs in the healthy and injured brain still need to be answered.^[14]

To tackle this issue, our laboratories developed highly fluorescent NPs which could be visualized in the brain *in vivo* by using intravital two-photon microscopy, as well as other imaging modalities.^[11] Among different nanoparticles, lipid NPs are particularly attractive for biological applications due to their natural non-toxic lipid components.^[5] Lipid nanoparticles (NPs) recently showed a great promise of nanoscale drug-delivery systems when used for the delivery of mRNA-based COVID-19 vaccines.^[15] In addition to mRNA, lipid NPs are also able to carry small molecules or contrast agents and were recently considered to have great potential for CNS drug-delivery due to their lipid structure.^[16] In the current study, we aimed to investigate the applicability of lipid nano-emulsion droplets (LNDs) after TBI, which are characterized by their simple preparation, high loading capacity, biodegradability, excellent safety profile, and great translational potential.^[17,18] LNDs are composed of ingredients generally recognized as safe (GRAS) for use in patients, such as natural oils and FDA-approved surfactants, thus having great potential in clinical translation. Moreover, it is known that lipid droplets can be visualized using electron microscopy.^[19] LNDs can be efficiently loaded with highly hydrophobic fluorescent dyes without any leakage in biological media. Previous work showed that hydrophobicity of the cationic dyes and their brightness can be significantly enhanced using bulky counterions,^[20] which enabled the preparation of dye-loaded polymeric NPs^[21,22] and their application *in vivo*.^[11,23] The counterion approach was also successfully used for loading cyanine 3 into LNDs, which yielded sufficiently bright fluorescence for detection in zebrafish *in vivo*.^[24] Moreover, using a FRET couple of

near-infrared dyes with bulky counterions, it was shown that LNDs, despite the liquid nature of their core, can preserve their integrity in the blood circulation for hours and enter xenografted tumors in an almost intact form.^[25]

Here, we loaded LNDs with the fluorescence dye rhodamine coupled to a bulky counter-ion in order to prevent dye quenching and to increase particle fluorescence. LNDs with a diameter of 30 and 80 nm were generated and used to track nanocarriers in the brain of living mice before and after TBI. Using *in vivo* imaging together with novel correlative light and electron microscopy (CLEM) techniques, we were able to unravel that LNDs cross the BBB at sites of microthrombus formation by endothelial transcytosis in the penumbra of a traumatic brain contusion and are subsequently taken up by neurons.

2. Experimental Section

2.1. Formulation of LNDs

The fluorescent LNDs was formulated using the nano-emulsification approach,^[26] where oil, surfactant, and dye are premixed together followed by the addition of water. In this approach, the ratio of surfactant to oil can control the size of the obtained LNDs in a broad range of 20–150 nm. The rhodamine (R18), a fluorescent dye, was loaded into the LNDs because of its good two-photon absorption properties, high brightness, and photostability.^[27] The counter-ion tetraphenylborate (TPB) was added to endow the cationic dye with higher hydrophobicity and thus enhance the encapsulation of rhodamine into the oil core of the LNDs^[24,25] and to minimize aggregation-induced quenching, thereby ensuring high single particle fluorescence.^[21,22] By varying the oil/surfactant ratio, LNDs with hydrodynamic diameters of 33 ± 3 and 85 ± 4 nm (mean \pm SD) as measured by dynamic light scattering (DLS), were prepared. LNDs loaded with 1 wt% R18/TBP with respect to oil had a fluorescence quantum yield of $17 \pm 2\%$ (Figure 1A,B). The observed good quantum yield confirmed solubilization of the dye in the oil core stabilized by the surfactant, without significant dye self-quenching. Considering the high number of loaded dye molecules per particle (84 and 1600 for 30 and 80 nm LNDs,

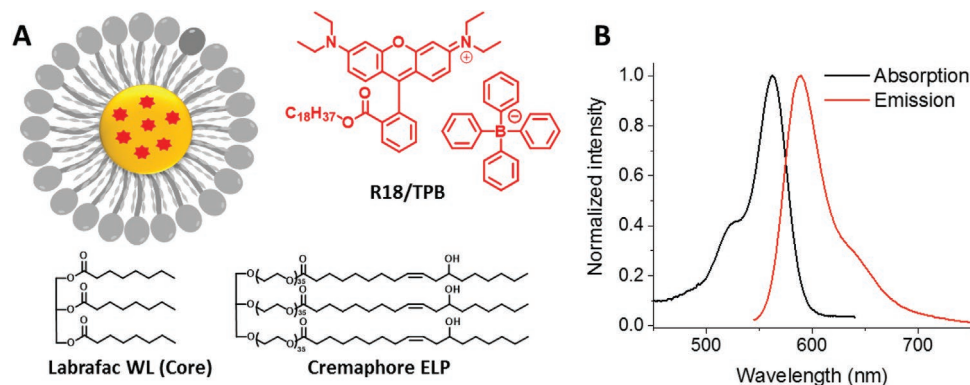


Figure 1. A) Schematic drawing of an LND consisting of the oil core (yellow; Labrafac WL), surfactant (grey; Cremaphore, Kolliphor ELP), and the fluorescent dye rhodamine bound to a hydrophobic counter-ion (R18/TPB). B) Normalized absorption and emission spectra of 30 nm LNDs. The LNDs were diluted 500-fold in water. The final dye concentration was 2 μ M.

respectively), the good quantum yield, the high extinction coefficient ($125\,000\text{ M}^{-1}\text{ cm}^{-1}$) and the two-photon absorption cross-section (200 GM),^[27] both LNDs preparations are expected to have a high enough fluorescence intensity to be tracked by intravital multi-photon microscopy *in vivo*.

2.2. In Vivo Imaging of LNDs in the Cerebral Circulation

30 or 80 nm LNDs were injected systemically via a femoral catheter in anesthetized mice and their distribution within the

cerebral circulation was assessed for two hours by intravital two-photon microscopy (2-PM) through an acute cranial window (Figure 2A). The fluorescent plasma marker fluorescein isothiocyanate (FITC)-dextran 2000 kDa was used to visualize cerebral vessels and served as a reference for vessel segmentation (Figure 2B; 0 min, FITC).

Shortly after injection, both 30 and 80 nm LNDs were observed in cerebral vessels (Figure 2B; 0 min, LND). Within the observation time of two hours, the LNDs of both sizes did not leave or occlude the lumen of any of the investigated vessel categories (pial arteries and veins, penetrating

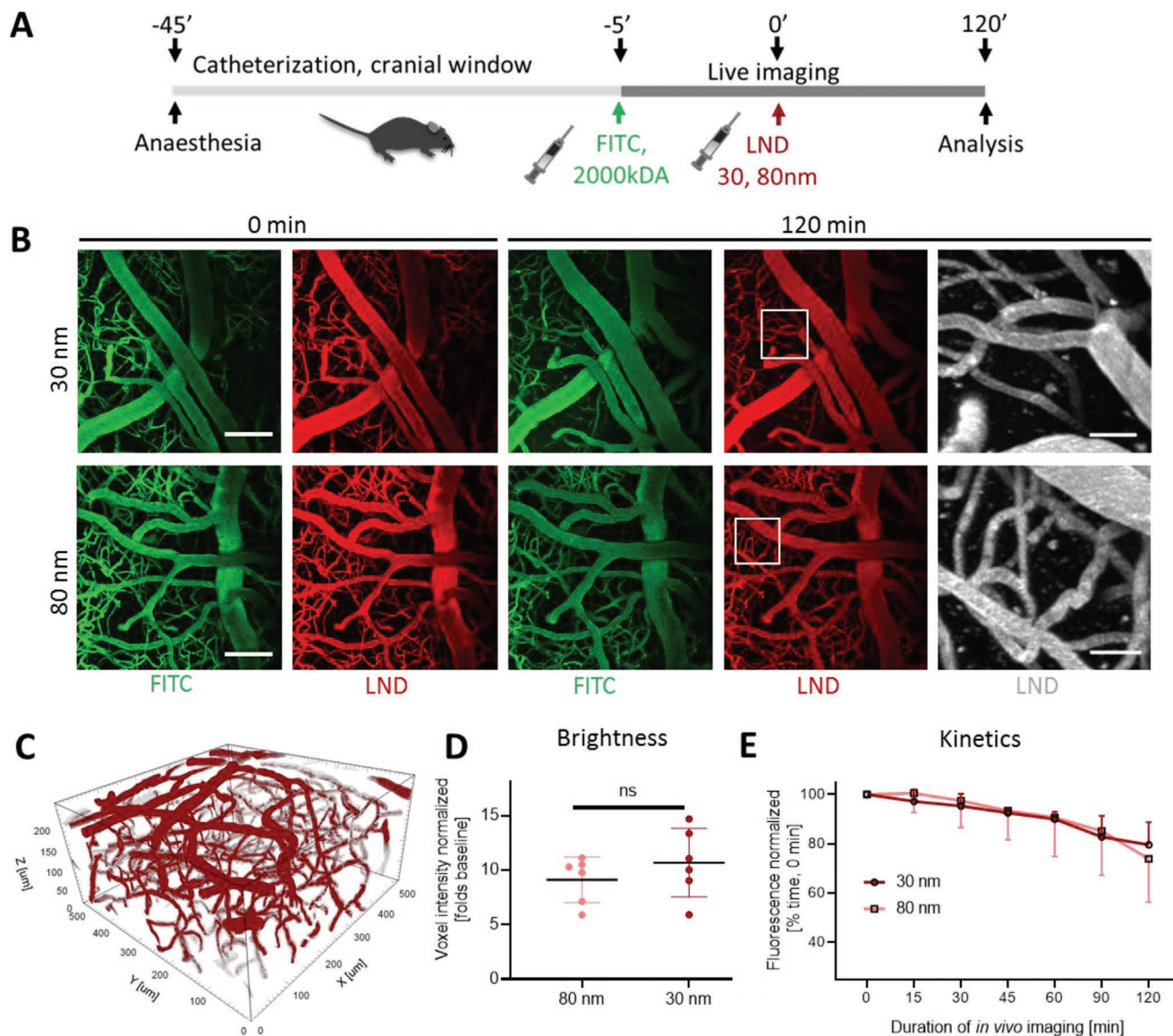


Figure 2. In vivo imaging of lipid nano-emulsion droplets (LND) in the cerebral circulation. A) Experimental design: surgical procedures (cranial window preparation, catheterization) and intravital imaging of injected LNDs. B) Maximum intensity projections of image Z-stacks were recorded by two-photon microscopy (2-PM) immediately after injection of LNDs and 120 min thereafter. Green – Fluorescein Isothiocyanate (FITC)-Dextran, 2000 kDa; red–LNDs 30, 80 nm; grey – zoomed vasculature with LNDs. Z-stack, 250 μm depth, maximum intensity projection. Scale bar – 100 μm . White outline–zoomed area of LNDs circulating in cerebral vessels. Scale bar – 20 μm . C) 3D view of LNDs circulating in cerebral vessels, processed with TubeAnalyst macros for Fiji software. D) 3D analysis of real-time brightness per voxel and E) Circulation kinetics of LNDs 30 nm versus 80 nm, using TubeAnalyst. Data presented as means \pm standard deviations. Statistical analysis: unpaired *t*-test (D) or two-way ANOVA (E) with Tukey correction for multiple comparison ($n = 6$ for each group); ns – non-significant ($p > 0.05$).

arterioles, cortical capillaries, or ascending veins; Figure 2B; 120 min).

To analyze the brightness of the circulating LNDs over time at the voxel level a 3D segmentation of the vascular tree using a Fiji macro TubeAnalyst (IRB Barcelona) was performed,^[28] in order to avoid artefacts of 2D projections (Figure 2C). The brightness of LNDs in vivo was independent of their size (Figure 2D) and remained relatively stable over time (Figure 2E). The brightness of the fluorescence signal of 80 nm LNDs two hours after injection was $73.9\% \pm 17.5$ of the value determined immediately after injection (baseline). 30 nm LNDs showed a comparable stability ($79.6\% \pm 9.1$; $p = 0.94$; two-way ANOVA; $n = 6$). FITC-dextran did not influence on LNDs brightness and circulation kinetics (Figure S1A–D, Supporting Information). Since single particle fluorescence was stable, the decreasing total fluorescence of circulating LNDs allows estimation of their plasma half-life.^[11] 30 and 80 nm LNDs had a circulation half-life of more than 2 h, a value comparable to previously published data for the laboratory for similar LNDs.^[25]

2.3. Extravasation of LNDs in the Mouse Brain After TBI

Animals were subjected to TBI using a well-established mouse model (controlled-cortical impact; CCI)^[29] and LNDs were injected systemically 60 min thereafter. This specific time point of particle injection was chosen since most TBI patients receive medical attention within the first hour after trauma. In order to investigate the biodistribution of LNDs in the cerebral vasculature and in the brain parenchyma, brains were perfusion fixed 30 or 120 min post-injection, removed, cut, and investigated by high-resolution confocal microscopy (Figure 3A).

First, the bio-distribution of 30 and 80 nm LNDs 90 min after TBI was analyzed, i.e., 30 min after injection. Cascade Blue (CB) dextran (10000 Da), a polysaccharide linked to a blue fluorescent molecule, which does not cross the BBB under physiological conditions, but is more than ten-fold smaller than LNDs, was injected along with LNDs to identify areas of the brain with a compromised BBB. Using this approach, areas were identified with a leaky BBB inside and around the cortical lesion, as well as in the hippocampus and the hypothalamus

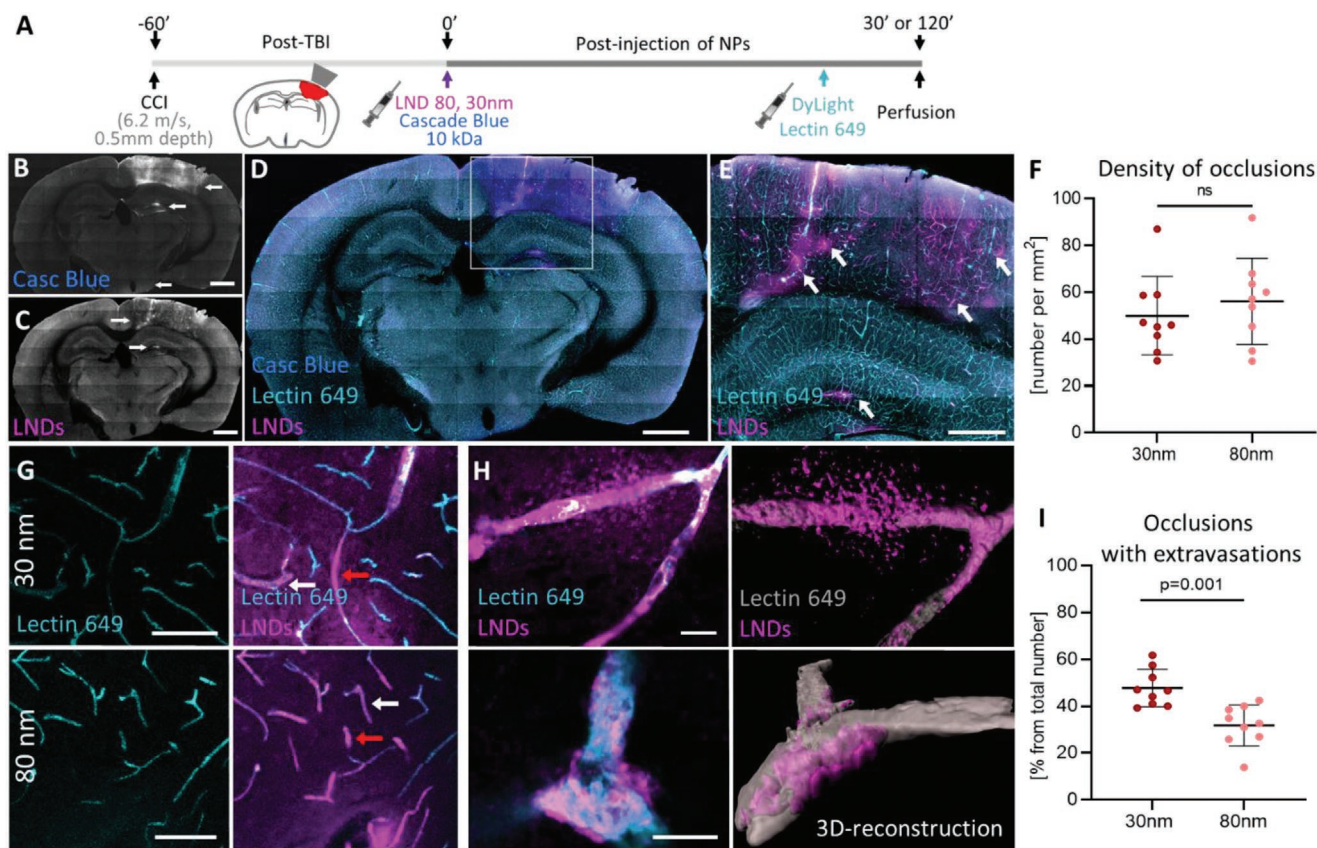


Figure 3. Lipid nano-emulsion droplets (LNDs) extravasate at sites of vascular occlusions following traumatic brain injury. A) Experimental design. CCI – controlled cortical impact; TBI – traumatic brain injury; LND – lipid nanodroplets. B,C,D) Coronal section of whole mouse injured brain 30 min after LNDs injection. E) Cortical lesion and hippocampus. Higher magnified area from D. White arrows: representative vascular occlusions (VO) with accumulated particles. 10x tile scan, maximum intensity projection of 60 μm z-stack. F) Quantification of the occlusions density in the lesion area. G) 30 nm and 80 nm NPs accumulated in VO of perilesional area. White arrow – vascular occlusions without extravasation; red arrows – extravasation. H) Scanned z-stack of extravasation of LNDs through the occluded microvessel. Left panel – maximum intensity projection; right panel – 3D-reconstruction. G&H – Upper panels: LNDs with 30 nm size, lower panels: LNDs with 80 nm size. Scale bars: B, C, D – 1 mm; E – 500 μm ; G – 100 μm ; H – 10 μm . I) Quantification of the fraction of occlusions with extravasation. F&I) Data presented as mean \pm standard deviation, 3 mice, 9 sections. Statistical analysis performed using GraphPrism, unpaired *t*-test; ns – non-significant ($p > 0.05$).

(Figure 3B; white arrows). Using the red fluorescence channel to identify LNDs, it was observed that deposition of LNDs of both sizes were co-localized with the areas of compromised BBB in the cortex and in the hippocampus (Figure 3C, white arrows, and 3D), suggesting that LNDs specifically accumulated in injured tissue. Higher magnification imaging revealed by co-localization with lectin, that the majority of 30 and 80 nm LNDs accumulated within the lumen of cerebral microvessels (Figure 3E; white arrows). Since LNDs did not accumulate spontaneously inside vessels (Figure 2B) and all non-adherent LNDs were removed from the circulation by perfusion fixation, the observed pattern of LNDs accumulation suggests that LNDs were incorporated into microvascular clots, so-called vascular occlusions (VOs). So far, the formation of VOs after brain injury was observed by histology and in the pial microcirculation by *in vivo* microscopy,^[30] however, little to nothing is known about the kinetics of their formation and their role in the pathophysiology of TBI. Since LNDs seem to label VOs, the discovery of LNDs' bio-distribution simultaneously elucidates spatial-temporal kinetics of VOs formation in the acute phase after TBI. Therefore, the VOs density and the influence of LNDs size on VO formation was next investigated. To investigate a therapeutically relevant area, the focus was on still perfused brain tissue surrounding the necrotic core of the contusion, the so-called traumatic penumbra.^[31] The penumbra as the tissue labelled by lectin was defined, i.e., the vascular dye injected minutes before sacrificing the animals, and having a compromised BBB as identified by CB extravasation (Figure S2A, Supporting Information; yellow dashed line). Using this approach, the volume of the traumatic penumbra to be around 2 mm² was calculated and to be the same in both investigated experimental groups (Figure S2B, Supporting Information; $p = 0.5662$, unpaired *t*-test, $n = 9$). Quantification within the traumatic penumbra showed that about 50 VOs were found per mm² and that the density of VOs was independent of the size of the injected LNDs (Figure 3F; $p = 0.4682$, unpaired *t*-test, $n = 9$). Only very few VOs were observed outside the traumatic penumbra (Figure 3D,E) and here again, the number of VOs was unrelated to LNDs size (Figure S2C, Supporting Information; $p = 0.9318$, unpaired *t*-test, $n = 9$). Moreover, no VOs were found in non-traumatized tissue of the contralateral hemisphere. These results suggest that LNDs are trapped within VOs while they form and are therefore suited to label and target VOs.

Interestingly, in some VOs, LNDs, remained inside the vessels (Figure 3G; white arrow), whereas in others the particles expanded beyond the vascular lumen (Figure 3G; red arrow). Using high-resolution confocal imaging and 3D-reconstruction, it was confirmed that in a number of VOs, large amount of LNDs were localized outside the vessel lumen, i.e., within the brain parenchyma (Figure 3H). In general, 30 nm LNDs tended to extravasate more readily than 80 nm particles (Figure 3H and Movie S1,2, Supporting Information). Quantification of this process revealed that in mice injected with 30 nm LNDs, almost half of the VOs were accompanied by extravasation, which was 1.5-fold more frequent than in animals injected with 80 nm particles (Figure 3I; $p = 0.001$, unpaired *t*-test, $n = 9$). This indicates that the permeability of the BBB increases at sites of VOs and allows 30 nm LNDs to extravasate into the brain parenchyma. Hence, these data indicate that LNDs do

not cross the healthy BBB, but are able to penetrate the BBB at sites of VOs suggesting that VOs alter the permeability of the BBB thereby facilitating the transport of LNDs into the brain parenchyma.

Next, we were interested to investigate the fate of LNDs which extravasated into the brain parenchyma. For this purpose, a similar experimental protocol was used as before, i.e., injection of LNDs after TBI, perfusion fixation, and investigation of the traumatic penumbra, but allowed the particles to circulate for two hours before the analysis (Figure 3A). In order to identify still perfused areas of the brain, animals were injected with the fluorescent vascular marker lectin some minutes before sacrifice (Figure 3A). Confocal microscopy of entire coronal sections revealed lectin-positive "perfused" and "non-perfused" areas thereby allowing identification of the lesion core and the penumbra (Figure 4A). LND fluorescence was associated with VOs and demonstrated that VOs with extravasations were predominantly found in the perilesional area, i.e., between the penumbra and the lesion core (Figure 4B; white arrow). Additionally, LND fluorescence was also detected within the brain parenchyma (Figure 4B; cyan arrow), suggesting that after extravasation LNDs diffuse into the surrounding brain tissue. The average tissue penetration depth of LNDs (Figure S3A, Supporting Information) was analyzed and found that 30 nm LNDs diffused twice as deep into the brain parenchyma as 80 nm LNDs, i.e., $233 \pm 99 \mu\text{m}$ (mean \pm SD) (Figure 4C; $p = 0.0007$, unpaired *t*-test, $n = 15$). When quantifying how many LNDs were left inside the vessel lumen, it was found that significantly more 80 nm LNDs than 30 nm to be associated with intravascular clots (Figure 4D; $p < 0.0001$, unpaired *t*-test, $n = 146$, $n = 341$), suggesting that 30 nm LNDs more readily extravasated into the brain parenchyma, while 80 nm preferentially stayed within the vessel lumen. The mean fluorescent intensity of the extravasate itself did not differ between 30 and 80 nm LNDs (Figure S3B; $p = 0.3415$, unpaired *t*-test, $n = 13$, $n = 15$). Altogether, these results suggest, that 30 nm LNDs more readily leave the intravascular compartment at sites of VOs and, once extravasated, penetrate deeper into the brain parenchyma than 80 nm LNDs.

In order to identify whether extravasated LNDs interact with neuronal cells, the brain parenchyma was investigated at larger magnification. 30 nm LNDs diffused homogeneously within the brain parenchyma (Figure 4E; upper row), while 80 nm LNDs gathered around their site of extravasation (Figure 4E; lower row). Extravasated 30 nm LNDs gathered in a fiber-like pattern with structures resembling synaptic boutons (Figure 4E; i, white arrows), suggesting accumulation of 30 nm LNDs in neurites, i.e., axons and/or dendrites. Although some 80 nm LNDs also accumulated in neurites (Figure S3C, Supporting Information; white arrow), these larger LNDs were predominantly taken up by perivascular cells surrounding VOs (Figure 4E ii, white arrows).

Interestingly, in non-perfused areas of the injured brain parenchyma, i.e., the core of the contusion, LNDs of both sizes were found within cells of different shapes (Figure S3C, Supporting Information; yellow arrows) which showed intense autofluorescence (Figure S3C, Supporting Information; green arrows). This suggests a random, non-specific accumulation of LNDs in dying cells.

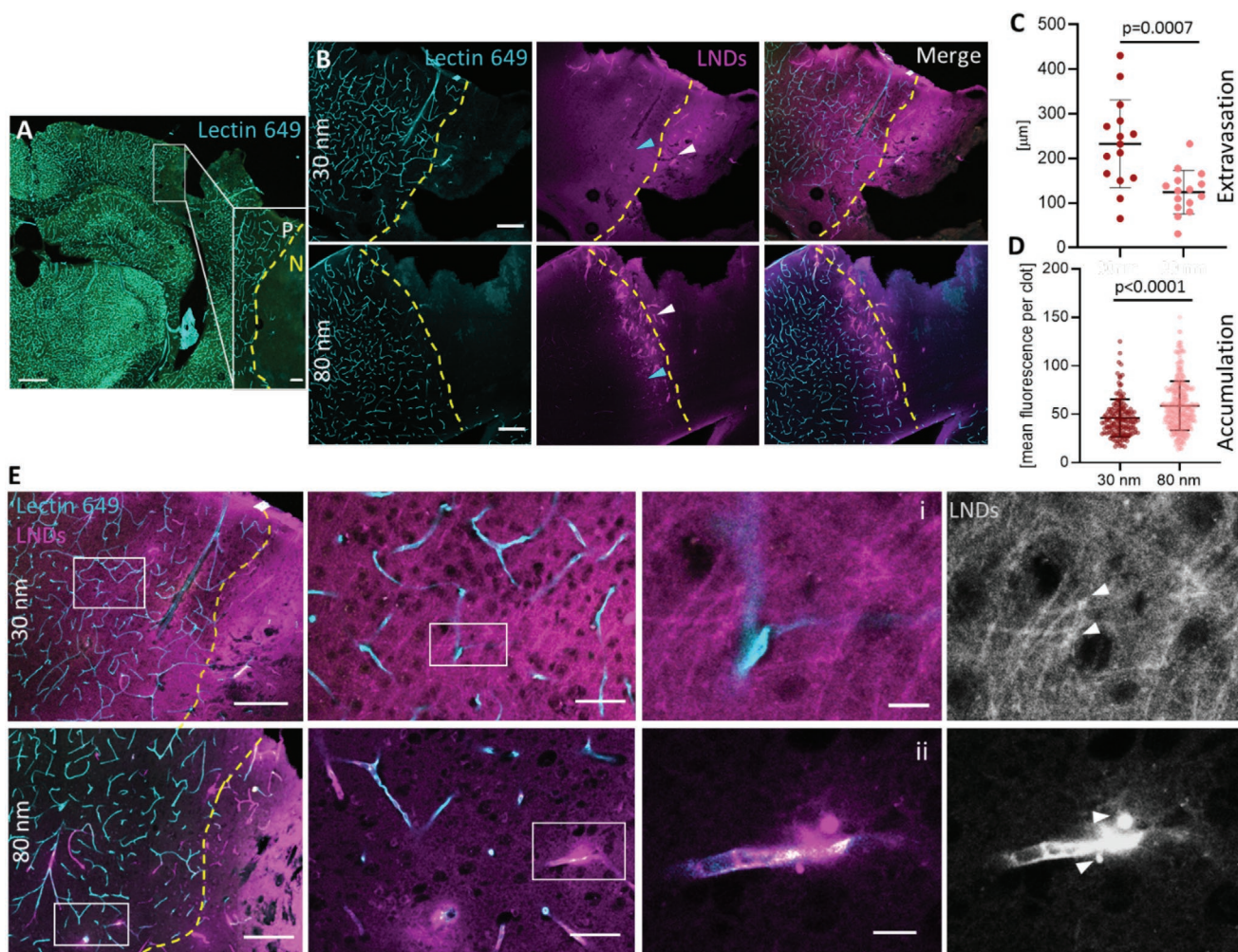


Figure 4. 120 min post-injection, 30 nm lipid nano-emulsion droplets (LNDs) diffuse deep into the brain parenchyma and are taken up by neurites. A) Representative coronal section of ipsilateral part of an injured mouse brain. Lectin, injected shortly before perfusion, shows the perfused area. Zoomed insert: yellow dashed line—a virtual border between perfused (P) and non-perfused (N) areas. B) Extravasation of LNDs into perfused brain tissue 120 min after injection. Upper panel shows a representative image of mouse with brain injury injected with 30 nm LNDs; lower 80 nm. White arrows—LNDs inside vascular occlusion (VO); cyan arrows—LNDs in brain tissue. C) Quantification of the depth of NPs diffusion into perfused tissue. Data presented as mean \pm SD, 3 mice, 9 sections, 15 regions of interest. D) Quantification of the amount of accumulated NPs inside VO. Data presented as mean \pm SD, 3 mice, 9 sections, 146 and 341 clots. Statistical analysis was performed using GraphPrism, an unpaired *t*-test. E) Representative 40x magnification images of perfused brain area from the mouse injected with 30 nm NPs (upper panel) and 80 nm NPs (lower panel). Inserts—zoomed regions from the perfused area. i) uptake of 30 nm LNDs by neuronal fibers. White arrows—structures suggestive axonal boutons. ii) uptake of 80 nm LNDs by cells surrounding the clots. White arrows—an accumulation of particles inside structures suggestive endosomes. Scale bars: (A) 500 μ m, insert 100 μ m; (B) 200 μ m; (E) 200 μ m, insert 50 μ m; (i, ii) 10 μ m.

To confirm these histological findings *in vivo*, an intravital two-photon microscopy was performed following a stab injury model (Figure S4A, Supporting Information). Using this approach, LNDs was confirmed of both sizes accumulate within VOs (Figure S4B–D, Supporting Information), that 80 nm LNDs do not extravasate (Figure S4E, Supporting Information; upper row), and that 30 nm LNDs cross the BBB and enter the brain parenchyma (Figure S4E, Supporting Information; lower row).

In order to verify the ability of LNDs to be taken up by and accumulate in neurons, *in vitro* experiments was performed. The primary cultured rat neurons were exposed to LNDs (Figure S5A, Supporting Information) and observed a gradual

accumulation of NPs of both sizes in neurites already 30 min after incubation. The accumulation continued until the end of the observation time (120 min) (Figure S5B,C,D, Supporting Information). Hence, these *in vitro* findings corroborate the *in vivo* data that LNDs, once extravasated, have a size-independent tropism towards neurons.

2.4. Mechanism of Vascular Permeability at Sites of Vascular Occlusions

The differential extravasation of smaller versus larger LNDs does not suggest a gross disruption of the integrity of cerebral

microvessels, but a rather specific increase in the permeability of the BBB. In order to exclude vascular disruption, erythrocytes were stained, cells known to be found in the brain parenchyma only when the integrity of the vascular wall is completely compromised. Microglia also were stained, which have recently been shown to become activated rapidly upon BBB opening.^[32] Since LNDs turned out to be sensitive to the immunostaining protocol, i.e., the procedure eradicated LND fluorescence, staining approach had to be adjusted. First, the fixed was scanned by unprocessed brain slice by confocal microscopy to identify LNDs and then immunohistochemistry was performed to identify red blood cells and microglia (Figure 5A). Using vessels as landmarks, and then confocal images were superimposed to acquire before and after immunostaining. This procedure allows fully maintaining of the signal from LNDs and to correlate the location of LNDs with markers of vascular disruption and BBB permeability. Applying this approach, analysis was focused on VOs in the traumatic penumbra, since the lesion core contained only dead tissue and mechanically destroyed vessels (Figure 5B,C). Within the penumbra, ROIs were investigated containing VOs with extravasations (Figure 5B,C (*)). Immunostaining with Ter119 revealed the absence of extravasated erythrocytes in the ROIs around the VOs, demonstrating that VOs in the traumatic penumbra were not associated with a loss of microvascular integrity and microbleeds (Figure 5D). In contrast, stalls of erythrocytes were observed inside the lumen of VOs. Moreover, it was found that every single VO visualized by LNDs in the whole brain slice, was co-localized with erythrocyte stalls inside the vessels (Figure 5D; white arrows), confirming that both 30 and 80 nm NPs accumulated inside microthrombi. Further, co-staining by Iba1 revealed that erythrocyte stalls were surrounded by microglial processes (Figure 5E; green arrows). This morphological microglial phenotype was recently defined as microglia “rosettes”,^[32] an early marker (20–60 min) of BBB opening. Such “rosettes” next to erythrocyte stalls in every single VO of the pericontusional area was found (Figure 5F,G; red arrows), suggesting that VOs cause BBB opening and/or leakage. Morphological analysis of microglia surrounding VOs (vascular occlusion-associated microglia; VOM) demonstrated activation of these cells (Figure S6, Supporting Information), i.e., the circularity index of microglia significantly increased in the vicinity of VOs as compared to microglia, which were not associated with VOs (non-VOM) (Figure 5H). VOM expanded their processes towards the VOs as indicated by the directionality index (Figure 5I). The size of particles did not play a role for this process. Furthermore, spatial correlative analysis revealed co-localization of intravascular VOs with erythrocyte stalls, activated VOMs, and intraparenchymal particle accumulation (Figure 5J,K; yellow arrows). Altogether, these findings implicate that LNDs of both sizes are trapped in VOs and afterwards cross the BBB in a size-dependent manner.

Next, the mechanisms of LNDs extravasation on the sub-cellular level were aimed to investigate. For this purpose, cerebral micro-vessels (lectin) and VOs (LNDs) were identified by confocal fluorescence microscopy and investigated the surrounding cells and tissues by low- and high-resolution electron microscopy (EM) on the same vibratome section (Figure 6A), correlating the fluorescence signals with the surrounding cellular ultrastructures.

The first finding using this approach was that LND fluorescence was preserved after tissue fixation with glutaraldehyde (Figure 6B). Accordingly, large confocal tile scans provided a map that allowed identification of areas of the brain containing fluorescent LNDs accumulated inside VO together with structural landmarks (vessels labelled by lectin) which enabled the re-identification of the very same VO by high- and low-resolution EM (Figure 6A). The imaged brain subregion was subsequently dissected and processed for EM using a standard en bloc embedding protocol.^[33] the ATUM (automated tape collecting ultramicrotomy) volume EM technique was applied to serially ultrathin section and collect the entire thickness of the sample for subsequent volume scanning electron microscopy (SEM). Low-resolution scanning ($0.2 \times 0.2 \times 2 \mu\text{m}$) was performed to cover the whole volume in order to screen for the ROI selected by light microscopy (Figure 6B,C). Using vessel patterns and section outlines as unique landmarks, the ROI from light microscopy was successfully re-located on the electron micrograph series (Figure S7A–E, Supporting Information) and selected for further high-resolution scanning (Figure 6D,E). SEM images obtained at different axial positions corresponded to the fluorescent signal from the acquired z-stack, reflecting a physical sectioning orientation, similar to the light microscopy focal planes (Figure S7F,G, Supporting Information). This correlative light electron microscopy procedure was applied to brain tissue obtained from both 30 and 80 nm LNDs injected mice. As such, two high-resolution SEM data sets of VOs were acquired (Figure 6F, Figure S7I, Supporting Information). Using this approach, individual LNDs inside VOs could be resolved by SEM (Figure 6G, Figure S7J, Supporting Information). Ultrastructure-based size analysis showed that in mice injected with 30 nm or 80 nm LNDs, the mean diameter was 27.16 and 62.21 nm, respectively (Figure S7K, Supporting Information), indicating that non-damaged LNDs successfully reached the VOs after systemic injection. The slight difference between the mean particle diameter assessed by DLS (33 ± 3 and 85 ± 4 nm respectively) and SEM most likely originates from the fact that particles visualized by SEM were not always cut through their maximal diameter. At sites of extravasation 30 nm LNDs were found within intracellular vesicles of endothelial cells (Figure 6H, white arrows), both individually and as aggregates (Figure 6H; insert). Moreover, the particles were observed outside the non-damaged vascular basal membrane, i.e., within the brain parenchyma (Figure 6H, yellow arrows), suggesting trans-cellular vesicular transport. Based on these results, a reconstruction of a VO with extravasated 30 nm LNDs to unravel their 3D-distribution (Figure 6I,J, Movie S3, Supporting Information) which confirmed 30 nm LNDs crossing the BBB via brain endothelial cells was performed. In contrast, 80 nm LNDs were not found to penetrate through the non-damaged endothelium. Instead, they accumulated inside VOs, typically forming highly-density deposits (Figure S7L, Supporting Information, red arrows). Further, it was found that 30 nm LNDs were internalized inside neurites in the healthy brain parenchyma (Figure S7E, Supporting Information; black arrow) as identified by lectin staining (Figure S7H, Supporting Information), a finding in line with these results obtained by light microscopy (Figure 4E,i). In tissue with compromised perfusion, LNDs were found in the cytoplasm of degenerated cells

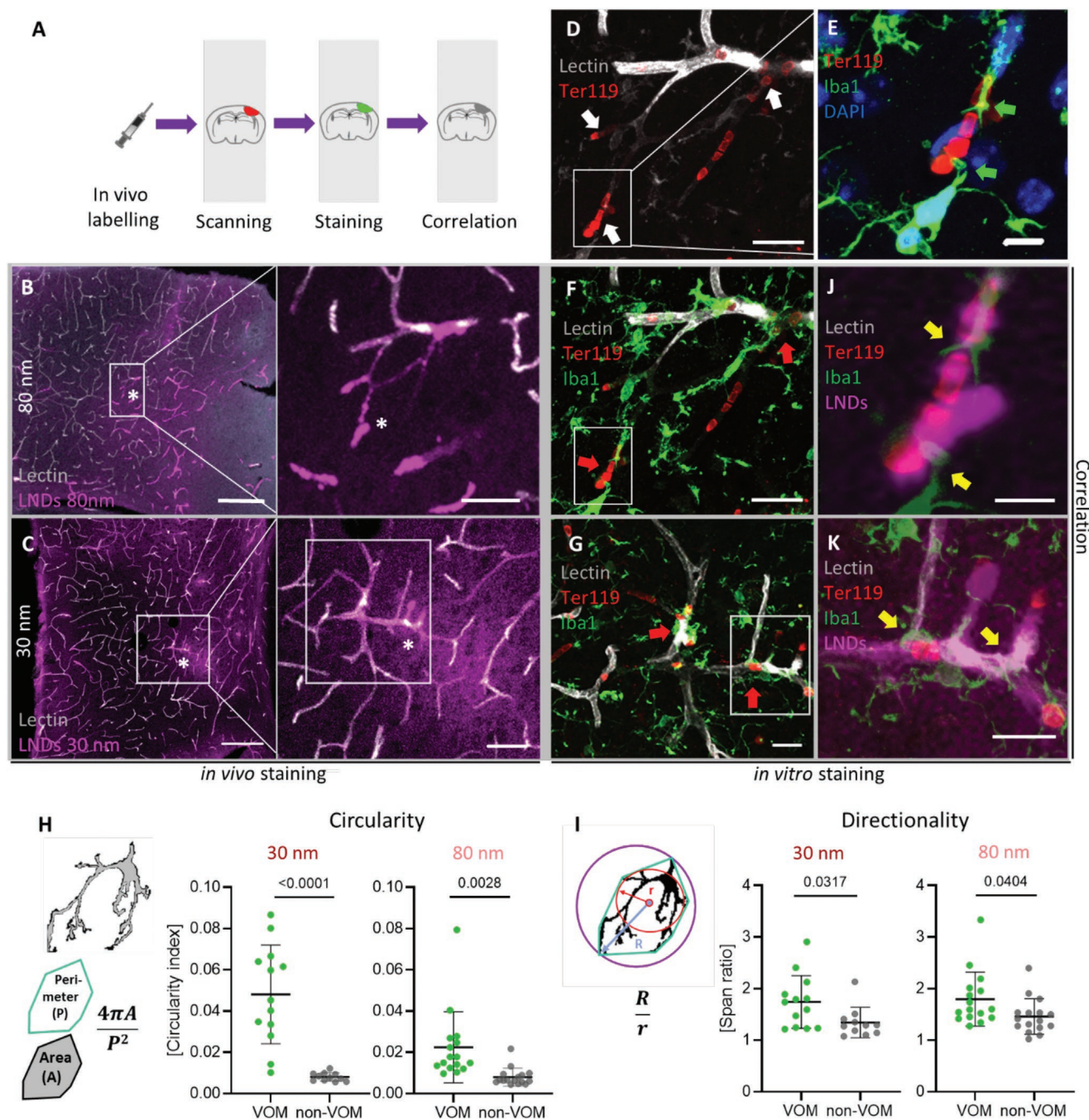


Figure 5. Vascular occlusion (VO)-induced extravasation of lipid nano-emulsion droplets (LNDs) is associated with activated microglia, but not with bleedings. A) The pipeline of correlation strategy of in vivo microscopy and post-fixed immunostainings. B,C) Representative confocal images of the cortical area of coronal sections of mice with TBI, 120 min post-injection with LNDs (magenta) 80 nm (B) or 30 nm (C). White rectangle—a region of interest (ROI), containing VO with accumulated and extravasated LNDs, located in the pericontusional area. Scale bars: 200 μ m; zoomed ROI 50 μ m. D) Matched ROI from B, stained with the erythrocyte marker Ter119 (red). Scale bar: 20 μ m. White arrows indicate the sites of VO with LNDs accumulations. White rectangle: ROI containing VO. E) Zoomed VO, stained with Ter119, the microglia marker Iba1, and DAPI. Microglia processes – green arrows. Scale bar: 10 μ m. F,G) Microglia processes surrounding VO with erythrocyte stalls (red arrows). Scale bar: 20 μ m. H&I). Morphological analysis of microglia (circularity (H) and directionality (I)). VOM: VO-associated microglia; non-VOM: microglia are not associated with VO, cells far from the VO. Data presented as mean \pm SD, $n = 15$. Statistical analysis was performed using GraphPrism, an unpaired t -test. J,K) Correlation of VO containing LNDs stained in vivo with in vitro post-fixed immunostaining shows that VO with accumulated LNDs contains erythrocyte stalls within vessel and microglia processes surrounding the vessel (yellow arrows). Scale bar: 10 μ m.

(Figure S7M, Supporting Information: i, ii), suggesting non-specific accumulation as also observed by light microscopy. Taken together, CLEM revealed that LNDs accumulate inside VO, but

only 30 nm LNDs were taken-up by brain endothelial cells, penetrate into pericontusional tissue via transcytosis, and are taken up by neurites. To confirm these findings, electron-dense

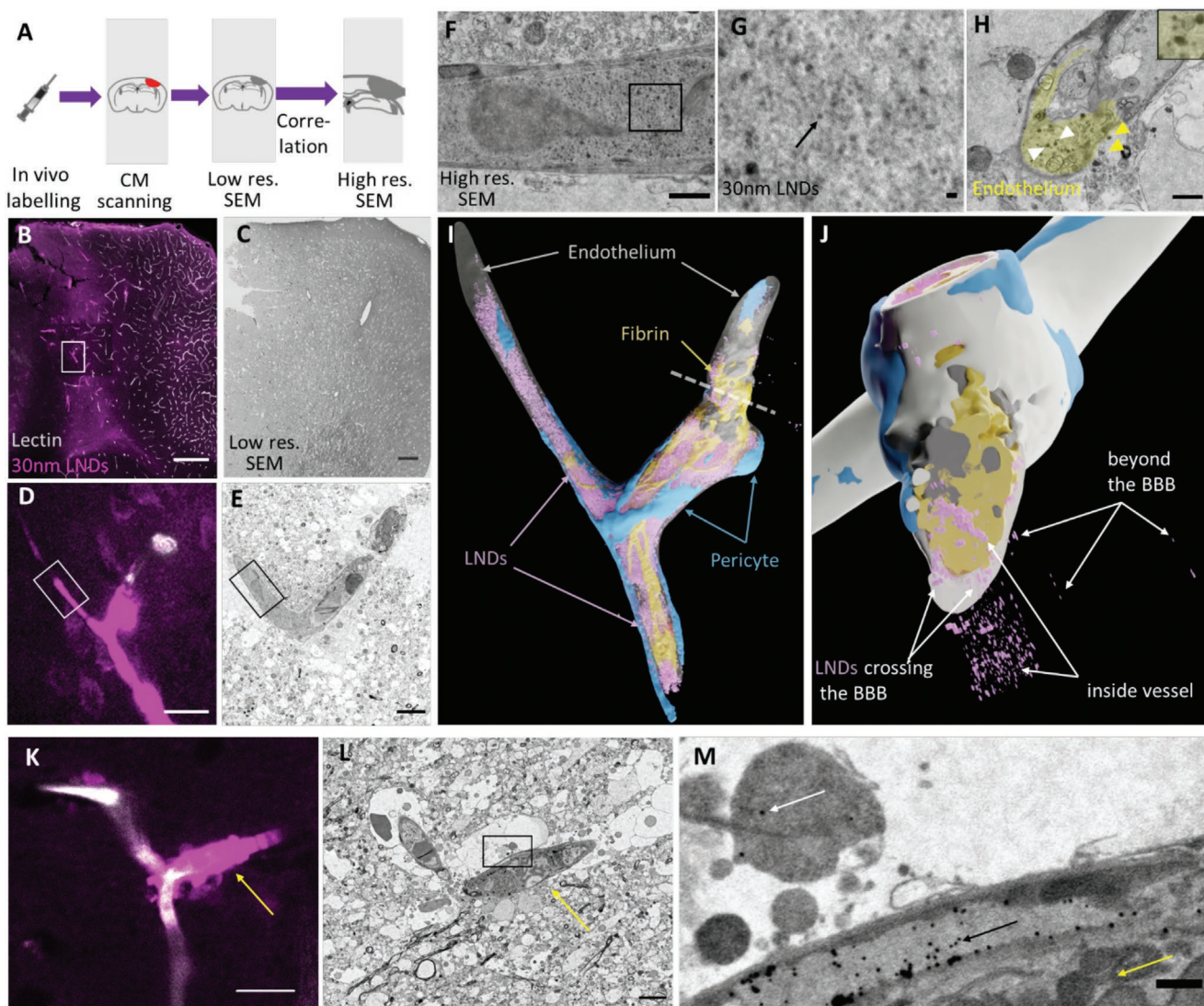


Figure 6. Correlative light electron microscopy (CLEM) of lipid nano-emulsion droplets (LNDs) reveals the extravasation of 30 nm particles through brain endothelial cells via vesicular transport. A) The pipeline of correlation strategy of confocal microscopy and electron microscopy after in vivo labelling. Confocal microscopy (CM); scanning electron microscopy (SEM); resolution (res.). B) Representative confocal image of the coronal cortical section of injured brain mouse, 120min post-injection of 30-nm LNDs (magenta), injected with DyLight Lectin (grey) minutes before sacrificing. Scale bar: 200 μ m. C) Representative scanning electron microscopy (SEM) low-resolution image of the pericontusional cortical area acquired on an ultrathin section of the same brain vibratome slice as in B. Scale bar: 100 μ m; D) Region of interest (ROI), containing vascular occlusion (VO) with accumulated and extravasated LNDs, located pericontusionally. Insert from B. Scale bar: 20 μ m. E) A higher resolution micrograph of ultrathin section correlated with D. Scale bar: 5 μ m. F) Representative high-resolution SEM of vessels containing 30 nm LNDs. Scale bar: 2 μ m; G) 30 nm LNDs (black arrow) inside VO. Zoomed ROI from F. Scale bar: 100 nm. H) 30 nm LNDs in the endothelial cytoplasm located inside vesicles (white arrow) and beyond the blood-brain barrier (BBB) in the brain parenchyma (yellow arrow). Scale bar: 1 μ m. I, J) Rendered 3D-reconstruction of the ROI from D, E. LNDs (magenta), endothelium (grey), endothelial blebs (dark grey), pericyte (blue), fibrin (yellow). K) Representative confocal image of perilesional VO (yellow arrow) with accumulated/extravasated LNDs (magenta) co-injected with 30 nm gold nanoparticles. Scale bar: 20 μ m. L) CLEM of VO from K. Scale bar: 5 μ m. M) Trans-endothelial transport of gold nanoparticles (black arrow) at the site of VO (yellow arrow) beyond the BBB (white arrow). Scale bar: 500 nm.

30 nm gold NPs (Figure S8A, Supporting Information) was used. Using the shape of the lesion and the brain vasculature as landmarks, VO containing fluorescent LNDs (Figure 6K,L; Figure S8B–D, Supporting Information, white arrow, black rectangle) could be re-identified. Using CLEM it was found that 30 nm gold NPs and fluorescent LNDs successfully reached the VO (Figure S8E, Supporting Information) without any morphological changes. At the site of perilesional VO with extravasated fluorescent LNDs (Figure 6K, yellow arrow), 30 nm gold NPs

were also transported across the BBB (Figure 6M, black arrow) through non-damaged brain endothelial cells with intact tight junctions (Figure S8G, Supporting Information, black arrow), implicating trans-endothelial transport. Using immunostaining for caveolin-1 (Cav-1), a marker for caveolae (Figure S9A,B, Supporting Information), it was found that endothelial cells adjacent to VOs highly expressed Cav-1, while endothelial cells far away from VOs did not (Figure S9C,D, Supporting Information). These findings suggest that at sites of VOs BBB

permeability increases due to the activation of transcytosis thereby mediating non-specific, but size-selective transcellular transport of nanoscale drug carriers across the BBB.

2.5. Methods

2.5.1. Lipid Nanodroplets

Dye loaded lipid nanoemulsions droplets were produced by spontaneous nanoemulsification by adapting previously described protocols.^[25] Briefly, the dye R18/TPB (prepared as described earlier^[21]) was first dissolved in LabrafacWL at 1% concentration by weight. Then, Kolliphor ELP (also called Cremophor ELP) was added, and the mixture was homogenized under magnetic stirring at 37 °C for 10 min up to complete homogenization. To obtain 30 nm LNDs, the amounts of LabrafacWL and Kolliphor ELP were 40 and 60 mg, respectively, whereas for 80 nm LNDs, they were 57 and 43 mg, respectively. Finally, LNDs were generated with the addition of Milli-Q water (230 mg). Hydrodynamic diameter was measured by DLS using a Zetasizer Nano ZSP (Malvern Instruments S.A., Worcester-shire, UK), using volume statistics. Absorption spectra were recorded on a Cary-5000 scan UV-visible spectrophotometer (Agilent, Santa Clara, CA, US), while emission spectra were recorded with a Spectrofluorometer FS5 (Edinburgh Instruments, Kirkton Campus, UK). The fluorescence spectra were corrected for detector response and lamp fluctuations. Fluorescence quantum yields of LNDs were measured using Rhodamine 101 in methanol as a reference (QY = 1.0) at excitation wavelength 530 nm.^[34]

2.5.2. Cranial Window

The acute cranial window was prepared as described previously.^[11] Briefly, 7-8-week old C57/Bl6N mice obtained from Charles River Laboratories (Kisslegg, Germany) were anesthetized intraperitoneally (ip) with a solution containing medetomidine (0.5 mg kg⁻¹), fentanyl (0.05 mg kg⁻¹), and midazolam (5mg kg⁻¹) (MMF). Throughout the experiment, animals were endotracheally intubated and ventilated in a volume-controlled mode (MiniVent 845, Hugo Sachs Elektronik, March-Hungstetten, Germany); body temperature was monitored and maintained by a rectal probe attached to a feedback-controlled heating pad. In a prone position, a rectangular 4 × 4 mm craniotomy was performed at the right fronto-parietal cortex under continuous cooling with saline. After removal of the bone flap and the dura mater, an exact fitting rectangular 4 × 4 mm cover glass of 0.175 μm thickness was placed upon the window and fixed onto the skull with dental cement.

2.6. Injection

For injection of LNDs and fluorescent vessel tracers, we used an established femoral arterial catheterization protocol.^[11] 7.5 μL g⁻¹ animal LnDs diluted 1:25 were injected for intravital imaging and 4 μL g⁻¹ for the CCI study. Dextran, Cascade Blue,

10 000 Da MW (Thermo Fisher Scientific, Waltham, Massachusetts, US) was injected to define the BBB damaged area, and Fluoresceinisothiocyanat-Dextran 0.5%, 2 000 000 MW (Merk, Darmstadt, and Germany) was injected to visualize the blood vessels in vivo, both in a dose of 3 μL g⁻¹ per mouse. DyLight 649 Labeled Lycopersicon Esculentum (Tomato) Lectin (Vector Laboratories, Burlingame, CA, US) 1 mg ml⁻¹ for labelling of blood vessels was injected in a quantity of 0.1 ml per mouse. 30 nm gold nanoparticles with density 1.00 g cm⁻³, methyl terminated, PEG 2000 coated (Sigma-Aldrich, St. Louis, Missouri, USA) were injected through femoral catheter into mouse in the same dose as LNDs (7.5 μL g⁻¹ animal).

2.7. Two-photon Image Acquisition

Two-photon images were scanned as previously described.^[11] Briefly, the anesthetized mouse with a cranial window was placed under an upright Zeiss LSM710 (Zeiss, Oberkochen, Germany) microscope and, after injection of FITC-dextran and localizing the region of interest (ROI) that represents most sizes and types of cerebral vessels, the baseline image was scanned. Next, immediately following injection of LnDs (30 nm or 80 nm), serial images were taken for 120 min. Ti:Sa laser (Chameleon Vision II) from 917 Coherent (Glasgow, Scotland) with an excitation wavelength of 830 nm and power of 5–22% was used for detection. GAASP detector with an LP < 570 nm filter with master gain 600 for the FITC channel and LP > 570 nm for the LnDs (rhodamine) channel with master gain 560 were used. Images were taken as z-stacks (250 μm, 512 × 512, 8 bit, objective: W Plan-Apochromat 20x/1.0 DIC D = 0.17 M27 75 mm).

2.8. 3D Analysis of LNDs Real-Time Circulation

Every acquired z-stack of intravital two-photon imaging was processed through the Fiji macro, TubeAnalyst (IRB Barcelona).^[28] First, using this algorithm, vessels from the z-stack were identified and segmented, obtaining the total vessel volume and vessel mask. Next, a generated mask was applied to the non-processed z-stack, which allowed them to exclude the background and keep the 3D fluorescence signal (Figure 2C). Finally, using Fiji, the total 3D fluorescence signal (integrated density) was calculated, which subsequently was divided by the total vessel volume, giving us fluorescence intensity per 1 mm³ of blood. Furthermore, in order to exclude fluctuations between animals and bleeding-through of FITC fluorescence, the obtained values were normalized to baseline and FITC.

2.9. Controlled Cortical Impact Model of Traumatic Brain Injury

Animals were subjected to experimental traumatic brain injury, using the previously described Controlled Cortical Impact (CCI) method.^[30,35] This model induces a highly reproducible lesion that shares many characteristics of human TBI. In short, after induction of anesthesia with buprenorphine (100 mg kg⁻¹ Bw) and isoflurane (4%, 30s), animals were sedated with 1,5–2,5% isoflurane in oxygen/air under continuous monitoring of

body temperature and heart rate. After right parietal craniotomy, the impact is directly applied to the intact dura with a pressure-controlled custom made CCI device (L. Kopacz, University of Mainz, Germany; 6 m s^{-1} , 0.5 mm penetration depth, 150 ms contact time). For sham-surgery, the CCI device tip is placed on the dura after craniotomy, but no impact is induced. After re-fixation of the skull plate and surgical closure, animals are ventilated with 100% oxygen until they regained consciousness, then were kept in an incubator at $34 \text{ }^{\circ}\text{C}$ and 60% humidity in order to prevent hypothermia. Stab injury was performed using a stereotactic frame as described previously.^[11]

2.10. Experiment Design

All animal experiments were approved by the Ethical Review Board of the Government of Upper Bavaria. The data were collected in accordance with the ARRIVE guidelines.^[36] Animal husbandry, health screens, and hygiene management checks were performed in accordance with Federation of European Laboratory Animal Science Associations (FELASA) guidelines and recommendations.^[37] 12 C57Bl/6N male mice, 23–25 g, underwent CCI as described above. 60 min post-CCI, mice were injected with 30 nm or 80 nm LnD ($n = 6$). Animals were divided into early (30 min) and late (120 min) post-injection groups. In the early group, LnDs injection was followed by Cascade Blue dextran (10 000 Da) injection, a very small and leaky dextran molecule that stains the injured area with opened BBB. In both groups, 5 min before sacrificing, animals received DyLight 649 Lectin to visualize perfused cerebral vessels. Animals were transcardially perfused with 4% PFA in deep anesthesia for immunohistochemical staining and with 2.5% of glutaraldehyde for correlative light-electron microscopy. For gold NPs and LNDs co-injection study, mouse ($n = 1$) was sacrificed 60 min post-injection. For all groups, the lesion area of fixed brains was subsequently cut in vibratome in rostral-caudal direction into $50 \mu\text{m}$ sections as previously described.^[38] Afterwards, three selected sections were immediately mounted by Fluoromount (Sigma, St. Luis, MO, US), covered by cover slip (Menzel Gläser, Braunschweig, Germany), and directly scanned under a confocal microscope.

2.11. Confocal Image Acquisition

Imaging was performed using confocal microscopy (ZEISS LSM 900, Carl Zeiss Microscopy GmbH, Jena Germany). For quantification of VO density, $10\times$ magnification (EC Plan-Neofluar $10\times/0.30$ M27) was used with an image matrix of 1024×1024 pixel, a pixel scaling of $0.2 \times 0.2 \mu\text{m}$ and a depth of 8 bit. Whole brain images were collected in z-stacks as tile scans with a slice-distance of $5 \mu\text{m}$ and a total range of $50 \mu\text{m}$. For a detailed analysis of extravasation, images were acquired with $40\times$ magnification (EC Plan-Neofluar $40\times/1.30$ Oil DIC M27) with an image matrix of 1024×1024 pixels, a pixel scaling of $0.2 \times 0.2 \mu\text{m}$, and a depth of 8 bit. For CLEM 3×3 tile z-stacks were acquired with $25\times$ magnification (LD LCI Plan-Apochromat $25\times/0.8$ Imm Korr DIC M27) and image matrix 1024×1024 pixels, a pixel scaling of $0.2 \times 0.2 \mu\text{m}$ and a depth of

8 bit. Specific regions of interest including the lesion site were collected in a single plane.

2.11.1. Occlusion Analysis

The occlusion density was analyzed in the area of co-localization of perfused vessels visualized by Lectin 649 and extravasated Cascade Blue (see above at Injection and Experimental Design). The size in mm^2 of this area was calculated at 3 coronal sections of each animal ($n = 3$, per group) using Fiji. Inside the area, the number of occlusions with accumulated nanoparticles was calculated per mm^2 . Statistical analysis was performed using GraphPrism, unpaired *t*-test. The vascular occlusions with accumulated NPs, where the fluorescent signal from rhodamine expanded over the border of the vessel (Lectin), were considered as VO with extravasation. The number of such VO was calculated versus the number of VO without extravasation at 3 coronal sections of each animal ($n = 3$, per group) using Fiji. Statistical analysis was performed using GraphPrism, unpaired *t*-test.

2.11.2. Extravasation

The border between perfused and non-perfused areas was drawn based on labelling by DyLight 649 Lectin. The length of the border was measured using Fiji and assigned as a perimeter of the lesion. The area of extravasation at the outer part of the perimeter was measured using Fiji and, subsequently divided on the length of the perimeter. The obtained value was assigned as a depth of extravasation into the non-injured tissue. The intensity of extravasation was computed as a mean grey value using Fiji. The depth and intensity of extravasation were calculated at 3 coronal sections of each animal ($n = 3$, per group). Statistical analysis was performed using GraphPrism, unpaired *t*-test.

2.11.3. Accumulation of LNDs in VO

The fluorescent intensity from the VO was calculated as a mean grey value using Fiji. The VOs from 3 coronal sections of each animal ($n = 3$, per group) was analyzed, in total 146 occlusions in the 30 nm group and 341 occlusions in 80 nm. Statistical analysis was performed using GraphPrism, unpaired *t*-test.

2.12. Correlative Immunohistochemistry

Coronal brain sections were prepared using a vibratome (Leica, Wetzlar, Germany) as described above. Since the lectin and LnDs were injected before perfusion of the mouse, no additional tissue processing was required. The lesion and perilesional area were scanned in the confocal microscope in order to obtain a non-affected signal from LnDs and vasculature. Afterwards, the sections were washed, blocked, and simultaneously stained with the primary antibody in buffer (1% bovine serum albumin, 0.1% gelatin from cold water fish skin, 0.5% Triton X-100 in 0.01 M PBS, pH 7.2–7.4) for 72h at $4 \text{ }^{\circ}\text{C}$. The following primary antibodies were used: iba-1 (rabbit, Wako,

#019-19741, 1:200), Ter119 (rat, Abcam, #ab91113, 1:100). After incubation, sections were washed in PBS and incubated with the following secondary antibodies: anti-rabbit coupled to Alexa Fluor 488 (goat anti-rabbit, Thermo Fisher Scientific, #A-11073, 1:200), anti-rat coupled to Alexa Fluor 594 (goat anti-guinea pig, Thermo Fisher Scientific, # A-11012, 1:200) in secondary antibody buffer (0.05% Tween 20 in 0.01 M PBS, pH 7.2–7.4). Nuclei were stained with 4',6-Diamidin-2-phenylindol (DAPI, Invitrogen, #D1306) 1:10000 in 0.01 M PBS. For caveolar staining conjugated Alexa Fluor 488 Anti-Caveolin-1 antibody was used (rabbit, Abcam, # ab185043, 1:50). Then the same tissue sections were scanned again and vasculature patterns were used as tissue landmarks in order to match VO of interest with Iba-1, Ter119, or Cav-1 staining.

2.12.1. Microglia Morphological Analysis

To assess microglia morphology, maximum intensity projection of iba-1 stained sections was used. Microglia for quantification were selected according to their proximity to VOs. Using vascular landmarks for orientation, ROIs containing VOs were selected in the pre-stained sections and later superimposed onto the same section stained with iba-1 to identify the neighboring microglia cells. A total of 11–16 cells per section and group were selected.

Fractal analysis was performed to indicate circularity and directionality using a modified protocol from Young and Morrison.^[39] Z-stack images were converted to a maximum intensity projection and cells were individually cut out using the polygon selection tool in ImageJ. Only cells that were entirely contained within the z-stack were selected. Images were then thresholded and binarized as well as resized to 600 × 600 pixels, keeping the original scale. Any speckles and debris around the cell were removed using the paintbrush tool. After converting binary images to outlines, fractal analysis was performed using the FracLac plugin for ImageJ.^[40] As described previously,^[39] the total number of pixels present in the cell image of either the filled or outlined binary image were calculated and later transformed to μm^2 (pixel area = 0208 μm^2). Cell circularity was calculated as $\text{Circularity} = 4\pi \cdot \text{Area} / \text{Perimeter}^2$.

The directionality of the cell was assessed by using the maximum and minimum span ratio across the convex hull.^[41]

2.13. Cell Culture Experiments

2.13.1. Mixed Cortical Cell Culture

Primary mixed cortical cultures were prepared from cortices of E17 embryonic Sprague-Dawley rat pups (Charles-River, kindly provided by Sabina Tahirovic) as previously described.^[11] In short, cortices were treated with DNaseI (10 $\mu\text{g mL}^{-1}$, Roche), triturated, and plated on round glass coverslips (≈ 275 cells mm^{-2}) coated with poly-D-lysine (0.1 mg mL^{-1}). Cells were plated in Neurobasal-A medium supplemented with 2% B-27, 2 mM GlutaMAX and 100 U mL^{-1} penicillin-streptomycin, containing 10 mM glucose and 1 mM pyruvate. Half of the media was exchanged after 6–24 h and subsequently two times

every week. Cells were cultured to maturity for 21 days in cell culture incubators at 37 °C and 5% CO₂/95% air).

2.13.2. Nanoparticle Uptake Assay

To assess neuronal uptake of nanoparticles, we added 10 μL of nanoparticles into each well at different time points and incubated them with cells for total incubation times of 30 min, 60 min, 90 min, and 120 min respectively. After incubation, cells were washed three times with 1x PBS and fixed for 15 min with 3.7% PFA/sucrose in PBS. Cells were washed three times with PBS and incubated for 10 min with 50 mM NH₄Cl to quench free aldehyde groups. After three further washes with PBS, cells were stored in PBS at 4 °C until staining.

2.13.3. Immunofluorescence Staining

Fixed mixed cortical cultures were blocked at RT for 1 h with a blocking buffer containing 0.2% BSA, 0.2% FBS, and 0.02% fish gelatin in PBS. Staining was performed by incubating cells with 1:1000 anti- β -Tubulin-III (mouse, T8578, Sigma) in blocking buffer for 3 h at RT. After three washes with PBS, anti-mouse coupled to Alexa Fluor 488 (donkey anti-mouse, 1:1000, 0.75 mg mL^{-1} , 715-546-150, Jackson Immuno Research) was incubated for 30 min. Nuclei were stained with 1:5000 DAPI for 5 min before final washes and mounting.

2.13.4. Confocal Image Acquisition

Imaging was performed using confocal microscopy (ZEISS LSM 900, Carl Zeiss Microscopy GmbH, Jena Germany). 3 × 3 tile z-stacks were acquired with 25 \times magnification (LD LCI Plan-Apochromat 25 \times /0.8 Imm Korr DIC M27) and image matrix 1024 × 1024 pixel, a pixel scaling of 0.2 × 0.2 μm and a depth of 8 bit.

2.14. Correlated light and ATUM Volume Scanning Electron Microscopy (CLEM)

Mice were perfused in fixative (4% PFA and 2.5% glutaraldehyde in 0.1 M sodium cacodylate buffer, pH 7.4; Science Services) and brains immersion fixed for 24 h, vibratome sectioned coronally and incubated for another 24 h in the same fixative and stored in PBS.

2.14.1. Confocal-mounting, Imaging Conditions, Demounting

The sections were stored in PBS at 4 °C until the start of the post embedding. The cortical region of interest (roughly 1.5 × 1.5 mm) was identified by comparison with the confocal overview scan and trimmed under a dissecting microscope using fine scalpels. We applied a standard rOTO en bloc staining protocol^[33] including postfixation in 2% osmium tetroxide (EMS), 1.5% potassium ferricyanide (Sigma) in 0.1 M sodium

cadodylate (Science Services) buffer (pH 7.4). Staining was enhanced by reaction with 1% thiocarbonylhydrazide (Sigma) for 45 min at 40 °C. The tissue was washed in water and incubated in 2% aqueous osmium tetroxide, washed and further contrasted by overnight incubation in 1% aqueous uranyl acetate at 4 °C and 2h at 50 °C. Samples were dehydrated in an ascending ethanol series and infiltrated with LX112 (LADD).

For the volume analysis, the block was trimmed by 200 μm at a 90° angle on each side using a TRIM90 diamond knife (Diatome) on the ATUMtome (Powertome, RMC). Serial sections were taken with a 35° ultra-maxi diamond knife (Diatome) at a nominal cutting thickness of 100 nm and collected on freshly plasma-treated (custom-built, based on Pelco easiGlow, adopted from M. Terasaki, U. Connecticut, CT), carbon nanotube (CNT) tape (Science Services). Covering the whole sample thickness of 80 μm and considering its unevenness after contrasting, 1000 sections were taken.

CNT tape stripes were assembled onto adhesive carbon tape (Science Services) attached to 4-inch silicon wafers (Siebert Wafer) and grounded by adhesive carbon tape strips (Science Services). EM micrographs were acquired on a Crossbeam Gemini 340 SEM (Zeiss) with a four-quadrant backscatter detector at 8 kV. In ATLAS5 Array Tomography (Fibics), wafer overview images were generated (1000 nm per pixel).

We acquired whole section low (0.5 × 0.5 × 2 μm) and medium resolution (0.1 × 0.1 × 2 μm) volumes of the area of interest (550 × 630 × 60 μm³) to facilitate relocation. Anatomical landmarks and vasculature patterns of single and summed sections were compared to the confocal data sets in Fiji.^[42] Within this volume, clots were selected for high-resolution imaging (clot C: 4 × 4 × 200 nm, 70 × 95 × 70 μm; clot A: 20 × 20 × 200 nm, 270 × 190 × 26 μm). Serial section data were aligned by a sequence of automated and manual processing steps in Fiji TrakEM2.^[42] VAST software was used for manual segmentation^[43] and Blender for rendering and movie generation^[44] of luminal and extraluminal structures of the neurovascular unit.

2.15. Statistical Analysis

Data are presented as mean ± standard deviation. For real-time brightness of NPs, an unpaired *t*-test was used (*n* = 6 mice); for circulation kinetics, two-way ANOVA with post-hoc Tukey correction for multiple comparisons was used (*n* = 6 mice). For the density of occlusions and extravasations in the TBI brain, an unpaired *t*-test was used (3 mice, 9 sections). For depth of particles penetration in penumbra, an unpaired *t*-test was used (3 mice, 9 sections, 15 regions of interest). For the number of accumulated NPs inside VOs, an unpaired *t*-test was used (3 mice, 9 sections, 146 and 341 clots). For morphological analysis of microglia (circularity and directionality), an unpaired *t*-test was used (*n* = 15 cells). F-test was used to test the equality of variances. Statistical analysis was performed using GraphPrism software.

3. Discussion

TBI is the leading cause of death and disability in children and young adults worldwide, however, adequate treatments to

prevent the development of post-traumatic neurodegeneration are still not available.^[3] Since targeted delivery of drugs into the healthy brain using nanomedicine is almost entirely inhibited by the BBB, understanding how acute brain injury influences the specific structural and functional characteristics of the BBB could reveal new opportunities for delivery of drugs to the CNS.^[45] For example, many studies showed that the BBB opens acutely after brain trauma and NPs accumulate in the injured brain,^[7,46,47] however, little is known about the underlying cellular mechanism. Experimental tools available so far did not have the spatial resolution to fully understand where exactly NPs were distributed after injury. Consequently, very little is known about the biodistribution and dynamics of NPs in the injured brain *in vivo*. In order to overcome these shortcomings, we developed a novel, super-bright NPs, which can be visualized by *in vivo* two-photon, and *ex vivo* confocal and electron microscopy, thus enabling us to study how, where, and when NPs cross the BBB.

In vivo measurement of permeability by direct imaging of fluorescent probes may suffer from dye leakage and dissociation of the probe from the fluorophore^[48] leading to false positive results. In order to avoid this, we used hydrophobic counterions for increasing the hydrophobicity of the resulting rhodamine dye, thus improving encapsulation and substantially reducing dye leakage.^[22] Additionally, the super-bright properties of NPs only unfold when the concentration of the rhodamine dye coupled with a tetraphenyl borate counter-ion is very high,^[21] therefore, the fluorescent signal from the fluorophore will be reduced by several orders of magnitude and become undetectable upon leakage. Further, in the current study, we used a whole range of correlative imaging techniques collecting the maximum amount of information, while preventing decomposition or washout of particles due to additional tissue processing. In addition, we also corrected for unspecific autofluorescence. Thus, a plethora of state-of-the-art imaging technologies was used to provide the most accurate readouts thereby avoiding unnecessary speculations.

The advantages and potential of rhodamine/counterion-based organic NPs we already demonstrated in different *in vivo* microscopy modalities,^[11,23] but have not yet been explored for LNDs. We chose lipid nanodroplets, since their simplicity in preparation and full biodegradability made them ideal as drug nanocarriers, which are composed of GRAS materials.^[17] Besides, lipid nanodroplets have already been proven stable and suitable for *in vivo* visualization when loaded with other bulky counterion-enhanced dyes.^[24]

We successfully visualized R18 loaded circulating particles *in vivo* using intravital two-photon microscopy, thereby demonstrating that the clearance of both sizes LNDs was relatively slow. Long circulation time for LNDs was suggested by other studies, implicating also that their integrity in the blood circulation was not affected.^[25] These similar elimination rates specifically for respective sizes are in line with previous studies using pegylated gold nanoparticles.^[49] Considering these features and the similar voxel brightness of 30 and 80 nm LNDs we could unbiasedly further study particles' biodistribution dynamics in the traumatized brain.

Although many studies, including our previous works, already showed retention of NPs in the injured brain^[11,47] or brain-specific pharmacological effect of the cargo carried by NPs

following the brain trauma,^[8,10] the exact site of particle accumulation as well as the cellular and subcellular mechanisms of transfer could not be specified so far. Using super-bright LNDs and advanced imaging techniques, we first demonstrated that already 30 min after systemic injection, LNDs specifically accumulated in VOs around the brain lesion in penumbra. These post-TBI VOs, most likely caused by spontaneous intravascular microthrombi, were previously observed in the cortex and hippocampus of TBI patients by histology^[50,51] and in pial microvessels of mice after experimental TBI by *in vivo* imaging.^[52] The formation of VOs is known to be a dynamic process, which starts during the first hour after TBI and continues at least for 72 h. However, direct observation of VOs within the parenchymal cerebral microcirculation *in vivo* and the spatial-temporal changes of their formation have not been reported yet and represent one of the most interesting pathophysiological findings of the current study. Apparently, post-traumatic VOs contain platelets, fibrinogen, and erythrocytes and are suggested to form in order to seal microendothelial leaks following TBI. At the same time, however, VOs may also contribute to further brain damage by causing or aggravating tissue ischemia.^[52–54] Our current results demonstrate that LNDs get trapped inside post-TBI VOs, thereby suggesting that, nanocarriers in general, and specifically 30–80-nm sized LNDs could be used to target VOs. Most other studies focusing on the biodistribution of NPs after TBI commonly investigated NPs larger than 100 nm.^[6,7,55] It is likely that these particles ended up inside VO, however, the imaging techniques used in these studies did not allow to resolve particle distribution at a cellular level. Thus, by showing for the first time that NPs accumulate inside VO after TBI, our data represent a novel approach to direct pharmacological substances to areas affected by microthrombosis.

Opening of the BBB for small molecules acutely and subacutely after TBI is well-documented both in humans and in preclinical animal models,^[56,57] and typically results in the formation of brain edema. In line with these studies, we could demonstrate using fluorescent dextran CB that BBB opening occurs at the cortical lesion, penumbra as well as hippocampus and hypothalamus 60–90 min post-CCI. It is known that extravasation of blood plasma occurs also in arterioles and venules, but mainly on the level of cerebral capillaries, as we could previously show by *in vivo* imaging.^[58] However, the undelaying cellular cause for the BBB leakage, also known as the opening of BBB, remained unclear. In the current study, we demonstrated that following TBI, the opening of the BBB is not diffusely distributed, but occurs at the site of VOs. We found that 30 nm LNDs readily passed the BBB already 30 min after injection at place where VOs formed. At later time points, 30 nm LNDs reached the brain parenchyma and accumulated in healthy neurons, while the bigger 80 nm LNDs remained within or close to VOs. Since the lesion core contains only non-functional and non-restorable damaged necrotic tissue, we focused our attention on the so-called penumbra, which is the area in-between healthy and necrotic tissue and therefore could potentially be treated therapeutically. Obviously, capillaries are damaged in the lesion core and BBB function is compromised so heavily that red blood cells, proteins, and LNDs leave the intravascular space specifically. Conversely, in the penumbra VO-associated BBB permeability was not accompanied by bleeding, since red blood cells were always confined to the vessel lumen. To identify

why the BBB became leaky to structures below 80 nm only at the site of VOs, we hypothesized that VOs may, for instance, activate inflammatory cells, which in turn release inflammatory mediators, e.g. bradykinin,^[59,60] which are known to increase vessel permeability. EM did not show any significant numbers of leukocytes within VOs, however, we found microglia surrounding VOs with increased permeability. VOs surrounded by activated microglia have recently been shown to occur at sites of increased BBB permeability after cerebral ischemia. Microglial activation was initiated by adenosine triphosphate released from astrocytes.^[32] Since VOs block the microcirculation, the area around the occlusion becomes hypoxic, thereby instantly inducing endothelial cell swelling.^[61] Subsequently, these swollen endothelial cells become permeable to blood-borne substances including circulating 30 nm LNDs. The presence of activated microglia as an indicator of increased BBB permeability suggests that LNDs extravasation can occur through sites of non-ruptured endothelium in non-destroyed capillaries. Thus, our results implicate both mechanistic insights of BBB opening after TBI and the new phenomenon that VOs may serve as gates for the delivery of nanomedicines to the brain parenchyma.

Another important mechanistic question is how exactly LNDs cross the BBB. Detection of LNDs by CLEM enabled us to directly compare 30 and 80 nm LNDs inside and outside VOs and to identify their cellular and subcellular localization. When focusing on pericontusional tissue where tight junctions and endothelial cells are still intact, 30-nm NPs were found in endothelial vesicles, while 80 nm LNDs mainly remained inside VOs, i.e., in the vessel lumen. These data suggest that 30 nm LNPs as well as gold NPs are transported across the BBB via vesicular transport, thereby indicating a size-related limitation of endothelial vesicular transport at the BBB. These data are well in line with previous *in vitro* and *in vivo* reports that particles between 10 and 50 nm are more readily taken up by endothelial cells than larger NPs.^[49,62,63] Additionally, we showed that VOs in the traumatic penumbra are associated with enhanced expression of Cav-1, a marker of caveolae. It was shown before that particle of 30 nm size are known to be preferentially transported by caveolae-mediated uptake^[64] and endothelial cell caveolae have a diameter of around 50 nm.^[65] Altogether our findings demonstrate that caveolar transport may play important role in the trafficking of 30 nm LNDs across the BBB.

Taken together, our current data suggest the following mechanisms how LNDs cross the BBB after TBI: in areas of the traumatized brain where endothelial cells are damaged, LNDs of both sizes enter the brain parenchyma through the disrupted endothelial barrier. This scenario is mainly observed in the terminally damaged core of the traumatic contusion. In areas of the traumatized brain where the endothelium is still intact, i.e., the still salvageable pericontusional penumbral tissue, 30 nm NPs transcellular cross the permeable BBB at VO site. Although the size of the transported NPs and high expression of Cav-1 at VO, suggest caveolar transport, further experiments are needed to identify the exact contribution of each molecular transport pathway, i.e., caveolin, clathrin, or non-specific cellular transport.^[5]

In addition to the mechanism of how LNDs cross the BBB after TBI, our current data also provides information about the fate of extravasated LNDs within the brain parenchyma. While the few extravasated 80 nm LNDs stayed near their VO of origin and did not move significantly beyond the vessel wall, 30 nm

particles penetrated much deeper into the brain parenchyma and reached neurons and neuronal processes. This finding is well in line with published data showing that the extracellular matrix (ECM) of the brain parenchyma consists of channels with a diameter of 20–60 nm.^[66,67] Thus, the diffusion of 80-nm LNDs was restricted by the pore size of the ECM, while 30 nm could easily diffuse along these channels and reach nearby neurons. Once reaching neurons, the uptake of LNDs was not size dependent, as suggested by our *in vitro* experiments, where LNDs were directly applied to cultured neurons. Hence, not cellular uptake but the diameter of NPs is the main parameter responsible for the presence of LNDs in neurons after TBI. These data provide crucial information about future targeting strategies for CNS drugs: for targeting VOs or paravascular structures, NPs with a diameter of >80 nm should be used, while when also parenchymal structures are supposed to be targeted the applied NPs should not be larger than 30 nm. Although we do not have direct evidence of whether the fully intact LNDs reached neurons, the clear difference in quality and speed of extravasation in between 30 and 80 nm LNDs additionally suggests that the detected signal originated mainly from NPs and not from the leaked dye. Our earlier studies with Förster resonance energy transfer (FRET)-based LNDs showed that intact NPs circulate for hours and enter vascularized tumor tissues in nearly intact form,^[25] which supports our conclusion. In the case of TBI, 30 nm LND could be used to transport pharmacologically active compounds to resolve microthrombi and protect still viable neurons from further damage.

4. Conclusion

The overall mechanism of LNDs extravasation following the brain trauma is summarized in **Figure 7**. LNDs injected intravenously stay within healthy vessels and have a plasma half life of several hours (Figure 7A). After TBI, 30 and 80 nm LNDs accumulate within VOs (Figure 7B). In areas with damaged BBB 30 and 80 nm LNDs extravasate into the brain parenchyma (Figure 7C), while in areas with preserved BBB only 30 nm transverse the intact endothelium by vesicular transport (Figure 7D). Once in the brain parenchyma, 30 nm LNDs diffuse over significant distances, reach nearby neurons, and are taken up into their cytoplasm (Figure 7E). The most important prerequisite for this process is that LNDs get trapped in VOs. Since the endothelial uptake of LNDs increases with decreasing velocity,^[68] it is comprehensive that a reduction of the velocity to zero within VOs greatly enhances the transport of LNDs across the damaged as well as the permeable BBB. It is important to note that we were able to observe extravasation events only around VOs, likely because the amount of extravasating LNDs is dependent on their concentration. Incidentally, LND concentration is extraordinarily high at the site of VOs due to their respective accumulation. It is possible that extravascular LNDs signal in other places of extravasation is below the detection limit of confocal microscopy, however, this also implies that the number of extravasated particles there is most likely negligible.

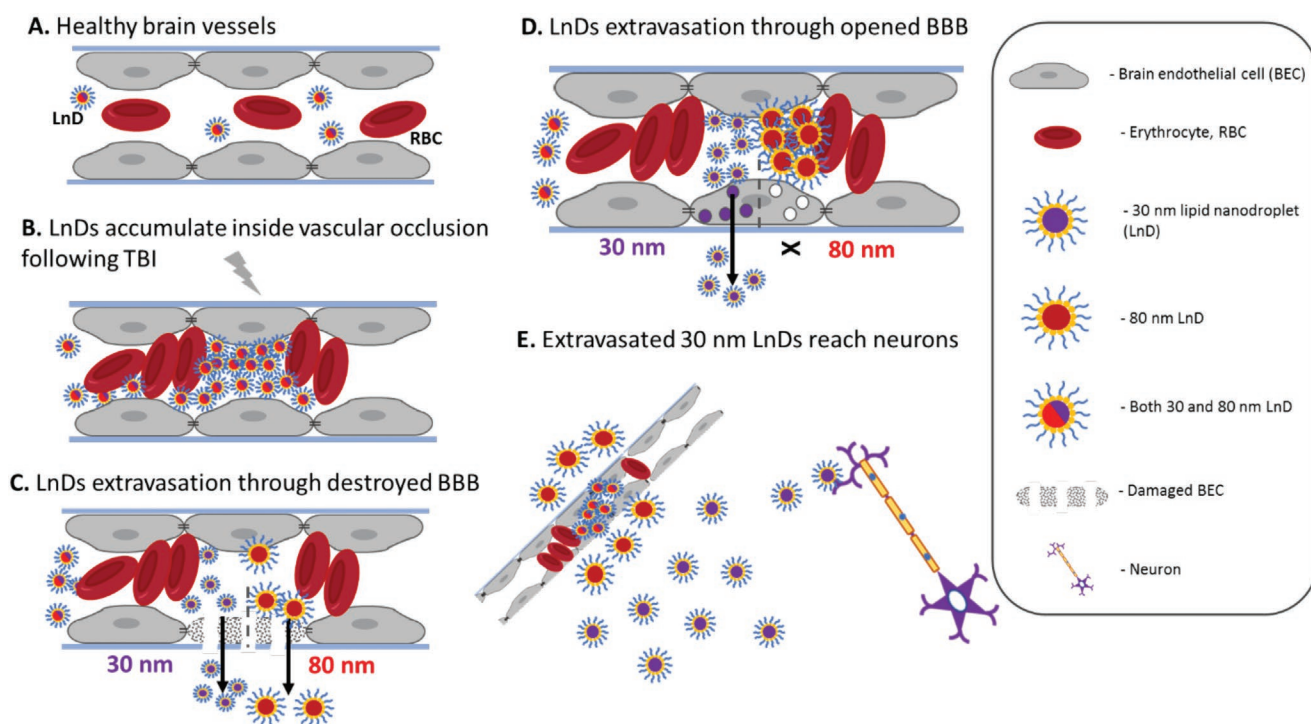


Figure 7. Mechanism (stages) of nanoparticles extravasation in penumbra through vascular occlusion following brain injury. A) Circulation of both 30 and 80 nm lipid nanodroplets in a healthy vessel and with closed blood-brain barrier (BBB). B) Formation of vascular occlusion (microthrombus) following the traumatic brain injury (TBI) provokes accumulation of LNDs between the trapped cells. C) 30 nm, but not 80 nm LNDs accumulated inside vascular occlusions are extravasating via intracellular vesicles of swollen endothelial cell (BBB is open). D) Both 30 nm and 80 nm LNDs are extravasating through damaged brain endothelial cell (BBB is destroyed). E) 80 nm LNDs, predominantly, stay around the vascular occlusion, while 30 nm LNDs reach the neurons in healthy areas.

The postulated mechanism shown above also sheds light on the so-called enhanced permeability-retention effect (EPR), previously used to explain how NPs reach brain following the brain trauma^[69] and could therefore deepen the understanding of nanoscale drug-delivery system extravasation in other types of acute brain injury or diseases associated with microthrombosis. However, the latter would need additional studies.

Taken together, our current data unravel the tissue, cellular and subcellular mechanism by which LNDs cross the BBB after TBI thereby paving the way for new application of LNDs as drug carriers for the treatment of the injured brain.

Supporting Information

Supporting Information is available from the Wiley Online Library or from the author.

Acknowledgements

The authors thank Georg Kislinger and Hanyi Jiang for the segmentation and rendering of the 3D EM model. This work was supported by the European Union Horizon 2020 research and innovation program under the Marie Skłodowska-Curie grant agreement No 794094, the European Research Council ERC Consolidator grant BrightSens 648528, the Agence National de Recherche J/C grant “Supertrack” ANR-16-CE09-0007, funded by the Deutsche Forschungsgemeinschaft (DFG, German Research Foundation) – projects number: 457586042, FOR2879; A03 – Mi 694/9-1 – 428663564; DFG under Germany’s Excellence Strategy within the framework of the Munich Cluster for Systems Neurology (EXC 2145 SyNergy—ID 390857198) and the TRR 274/1 2020 – 408885537 (project Z01).

Open access funding enabled and organized by Projekt DEAL.

Conflict of Interest

The authors declare no conflict of interest.

Data Availability Statement

The data that support the findings of this study are available from the corresponding author upon reasonable request.

Keywords

blood-brain barrier, brain injury, correlative light-electron microscopy, drug delivery, nanoparticles

Received: January 15, 2022

Revised: March 10, 2022

Published online: April 5, 2022

- [1] L. Wilson, L. Horton, K. Kunzmann, B. J. Sahakian, V. F. J. Newcombe, E. A. Stamatakis, N. von Steinbuechel, K. Cunitz, A. Covic, A. Maas, D. V. Praag, D. Menon, *J. Neurol. Neurosurg. Psychiatry* **2021**, *92*, 407.
- [2] D. H. Smith, V. E. Johnson, W. Stewart, *Nat. Rev. Neurol.* **2013**, *9*, 211.
- [3] S. Kabadi, A. Faden, *Int. J. Mol. Sci.* **2014**, *15*, 1216.

- [4] R. Alyautdin, I. Khalin, M. I. Nafeeza, M. H. Haron, D. Kuznetsov, *Int. J. Nanomedicine* **2014**, *9*, 795.
- [5] M. J. Mitchell, M. M. Billingsley, R. M. Haley, M. E. Wechsler, N. A. Peppas, R. Langer, *Nat. Rev. Drug Discovery* **2021**, *20*, 101.
- [6] W. Li, J. Qiu, X.-L. Li, S. Aday, J. Zhang, G. Conley, J. Xu, J. Joseph, H. Lan, R. Langer, R. Mannix, J. M. Karp, N. Joshi, *Sci. Adv.* **2021**, *7*, eabd6889.
- [7] L. J. Cruz, M. A. Stammes, I. Que, E. R. Van Beek, V. T. Knol-Blankevoort, T. J. A. Snoeks, A. Chan, E. L. Kaijzel, C. W. G. M. Löwik, *J. Control Release* **2016**, *223*, 31.
- [8] E. J. Kwon, M. Skalak, R. Lo Bu, S. N. Bhatia, *ACS Nano* **2016**, *10*, 7926.
- [9] D. Yoo, A. W. Magsam, A. M. Kelly, P. S. Stayton, F. M. Kievit, A. J. Convertine, *ACS Nano* **2017**, *11*, 8600.
- [10] I. Khalin, R. Alyautdin, T. W. Wong, J. Gnanou, G. Kocherga, J. Kreuter, *Drug Delivery* **2016**, *23*, 3520.
- [11] I. Khalin, D. Heimbürger, N. Melnychuk, M. Collot, B. Groschup, F. Hellal, A. Reisch, N. Plesnila, A. S. Klymchenko, *ACS Nano* **2020**, *14*, 9755.
- [12] P. Henrich-Noack, D. Nikitovic, M. Neagu, A. O. Docea, A. B. Engin, S. Gelperina, M. Shtilman, P. Mitsias, G. Tzanakakis, I. Gozes, A. Tsatsakis, *Nanomedicine* **2019**, *17*, 359.
- [13] L. L. Israel, A. Galstyan, E. Holler, J. Y. Ljubimova, *J. Controlled Release* **2020**, *320*, 45.
- [14] J. Kreuter, *Adv. Drug Delivery Rev.* **2014**, *71*, 2.
- [15] A. B. Vogel, I. Kanevsky, Y. Che, K. A. Swanson, A. Muik, M. Vormehr, L. M. Kranz, K. C. Walzer, S. Hein, A. Güler, J. Loschko, M. S. Maddur, A. Ota-Setlik, K. Tompkins, J. Cole, B. G. Lui, T. Ziegenhals, A. Plaschke, D. Eisel, S. C. Dany, S. Fesser, S. Erbar, F. Bates, D. Schneider, B. Jesionek, B. Sängler, A.-K. Wallisch, Y. Feuchter, H. Junginger, S. A. Krumm, et al., *Nature* **2021**, *592*, 283.
- [16] D. M. Teleanu, C. Chircov, A. M. Grumezescu, R. I. Teleanu, *Pharmaceutics* **2019**, *11*, 101.
- [17] N. Anton, J. - P. Benoit, P. Saulnier, *J. Control Release* **2008**, *128*, 185.
- [18] A. S. Klymchenko, F. Liu, M. Collot, N. Anton, *Adv. Healthcare Mater.* **2021**, *10*, 2001289.
- [19] J. Marschallinger, T. Iram, M. Zardeneta, S. E. Lee, B. Lehallier, M. S. Haney, J. V. Pluvinage, V. Mathur, O. Hahn, D. W. Morgens, J. Kim, J. Tevini, T. K. Felder, H. Wolinski, C. R. Bertozzi, M. C. Bassik, L. Aigner, T. Wyss-Coray, *Nat. Neurosci.* **2020**, *23*, 194.
- [20] A. S. Klymchenko, E. Roger, N. Anton, H. Anton, I. Shulov, J. Vermot, Y. Mely, T. F. Vandamme, *RSC Adv.* **2012**, *2*, 11876.
- [21] A. Reisch, P. Didier, L. Richert, S. Oncul, Y. Arntz, Y. Mély, A. S. Klymchenko, *Nat. Commun.* **2014**, *5*, 4089.
- [22] B. Andreiuk, A. Reisch, E. Bernhardt, A. S. Klymchenko, *Chem. Asian J.* **2019**, *14*, 836.
- [23] I. Khalin, C. Severi, D. Heimbürger, A. Wehn, F. Hellal, A. Reisch, A. S. Klymchenko, N. Plesnila, *Nanomedicine: Nanotechnol., Biol. Med.* **2022**, *40*, 102511.
- [24] V. N. Kilin, H. Anton, N. Anton, E. Steed, J. Vermot, T. F. Vandamme, Y. Mely, A. S. Klymchenko, *Biomaterials* **2014**, *35*, 4950.
- [25] R. Bouchaala, L. Mercier, B. Andreiuk, Y. Mély, T. Vandamme, N. Anton, J. G. Goetz, A. S. Klymchenko, *J. Control Release* **2016**, *236*, 57.
- [26] N. Anton, T. F. Vandamme, *Pharm. Res.* **2011**, *28*, 978.
- [27] C. Xu, W. W. Webb, *J. Opt. Soc. Am. B* **1996**, *13*, 481.
- [28] J. S. Jeon, S. Bersini, J. A. Whisler, M. B. Chen, G. Dubini, J. L. Charest, M. Moretti, R. D. Kamm, *Integ. Biology: Quant. Biosci. Nano Macro* **2014**, *6*, 555.
- [29] A. C. Wehn, I. Khalin, M. Duering, F. Hellal, C. Culmsee, P. Vandenabeele, N. Plesnila, N. A. Terpolilli, *Acta Neuropathol. Commun.* **2021**, *9*, 138.
- [30] S. M. Schwarzmaier, S.-W. Kim, R. Trabold, N. Plesnila, *J. Neurotrauma* **2010**, *27*, 121.

- [31] H.-M. Wu, S.-C. Huang, P. Vespa, D. A. Hovda, M. Bergsneider, *J. Neurotrauma* **2013**, *30*, 352.
- [32] P. Mastorakos, N. Mihelson, M. Luby, S. R. Burks, K. Johnson, A. W. Hsia, J. Witko, J. A. Frank, L. Latour, D. B. McGavern, *Nat. Neurosci.* **2021**, *24*, 245.
- [33] G. Kislinger, H. Gnägi, M. Kerschensteiner, M. Simons, T. Misgeld, M. Schifferer, *STAR Protoc.* **2020**, *1*, 100232.
- [34] T. Karstens, K. Kobs, *J. Phys. Chem.* **1980**, *84*, 1871.
- [35] S. Cheng, X. Mao, X. Lin, A. Wehn, S. Hu, U. Mamrak, I. Khalin, M. Wostrack, F. Ringel, N. Plesnila, N. A. Terpolilli, *J. Neurotrauma* **2021**, *1*, 1572.
- [36] C. Killkenny, W. J. Browne, I. C. Cuthill, M. Emerson, D. G. Altman, *PLoS Biol.* **2010**, *8*, e1000412.
- [37] J. Guillen, *J. Am. Assoc. Lab. Anim. Sci.* **2012**, *51*, 311.
- [38] M. Ghosh, M. Balbi, F. Hellal, M. Dichgans, U. Lindauer, N. Plesnila, *Ann. Neurol.* **2015**, *78*, 887.
- [39] K. Young, H. Morrison, *J. Vis. Exp.* **2018**, *5*, 57648.
- [40] A. Karperien, *FracLac for ImageJ*. 1999–2013.
- [41] M. D. M. Fernández-Arjona, J. M. Grondona, P. Granados-Durán, P. Fernández-Llebrez, M. D. López-Ávalos, *Front. Cell Neurosci.* **2017**, *11*, 235.
- [42] J. Schindelin, I. Arganda-Carreras, E. Frise, V. Kaynig, M. Longair, T. Pietzsch, S. Preibisch, C. Rueden, S. Saalfeld, B. Schmid, J.-Y. Tinevez, D. J. White, V. Hartenstein, K. Eliceiri, P. Tomancak, A. Cardona, *Nat. Methods* **2012**, *9*, 676.
- [43] D. R. Berger, H. S. Seung, J. W. Lichtman, *Front. Neural Circuits* **2018**, *12*, 88.
- [44] A. Brito, Blender Quick Start Guide: 3D Modeling, Animation, and Render with Eevee in Blender 2.8., *Packt Publishing* **2018**.
- [45] M. Nowak, M. E. Helgeson, S. Mitragotri, *Adv. Ther.* **2020**, *3*, 1900073.
- [46] L. E. Waggoner, M. I. Madias, A. A. Hurtado, E. J. Kwon, *AAPS J.* **2021**, *23*, 100.
- [47] V. N. Bharadwaj, J. Lifshitz, P. D. Adelson, V. D. Kodibagkar, S. E. Stabenfeldt, *Sci. Rep.* **2016**, *6*, 29988.
- [48] R. Münster, K. Kristensen, D. Pedersbæk, J. B. Larsen, J. B. Simonsen, T. L. Andresen, *Nanoscale* **2018**, *10*, 22720.
- [49] N. Hoshyar, S. Gray, H. Han, G. Bao, *Nanomedicine* **2016**, *11*, 673.
- [50] S. C. Stein, D. I. Graham, X.-H. Chen, D. H. Smith, *Neurosurgery* **2004**, *54*, 687.
- [51] S. C. Stein, X.-H. Chen, G. P. Sinson, D. H. Smith, *J. Neurosurgery* **2002**, *97*, 1373.
- [52] S. M. Schwarzmaier, C. De Chaumont, M. Balbi, N. A. Terpolilli, C. Kleinschnitz, A. Gruber, N. Plesnila, *J. Neurotrauma* **2016**, *33*, 1634.
- [53] C. Albert-Weissenberger, S. Hopp, B. Nieswandt, A.-L. Sirén, C. Kleinschnitz, C. Stetter, *J. Neuroimmunol.* **2019**, *326*, 9.
- [54] D. Lu, A. Mahmood, A. Goussev, C. Qu, Z. G. Zhang, M. Chopp, *J. Neurotrauma* **2004**, *21*, 1756.
- [55] A. Zinger, S. Soriano, G. Baudo, E. D. Rosa, F. Taraballi, S. Villapol, *Adv. Funct. Mater.* **2021**, *31*, 2100722.
- [56] D. K. Sandsmark, A. Bashir, C. L. Wellington, R. Diaz-Arrastia, *Neuron* **2019**, *103*, 367.
- [57] Y. Wu, H. Wu, X. Guo, B. Pluimer, Z. Zhao, *Front. Physiol.* **2020**, *11*, 1030.
- [58] S. M. Schwarzmaier, M. Gallozzi, N. Plesnila, *J. Neurotrauma* **2015**, *32*, 990.
- [59] K. Zweckberger, N. Plesnila, *Neurosci. Lett.* **2009**, *454*, 115.
- [60] N. Plesnila, J. Schulz, M. Stoffel, J. Eriskat, D. Pruneau, A. Baethmann, *J. Neurotrauma* **2001**, *18*, 1049.
- [61] M. Krueger, I. Bechmann, K. Immig, A. Reichenbach, W. Härtig, D. Michalski, *J. Cereb. Blood Flow Metab.* **2015**, *35*, 292.
- [62] S. Egloff, A. Runser, A. Klymchenko, A. Reisch, *Small Methods* **2021**, *5*, 2000947.
- [63] E. T. Ahrens, J. W. M. Bulte, *Nat. Rev. Immunol.* **2013**, *13*, 755.
- [64] Z. Wang, C. Tiruppathi, R. D. Minshall, A. B. Malik, *ACS Nano* **2009**, *3*, 4110.
- [65] S. A. Predescu, D. N. Predescu, A. B. Malik, *Am. J. Physiol.* **2007**, *293*, L823.
- [66] P. Kamali-Zare, C. Nicholson, *Basic Clin. Neurosci.* **2013**, *4*, 282.
- [67] R. G. Thorne, C. Nicholson, *Proc. Natl. Acad. Sci. USA* **2006**, *103*, 5567.
- [68] Y. Y. Chen, A. M. Syed, P. MacMillan, J. V. Rocheleau, W. C. W. Chan, *Adv. Mater.* **2020**, *32*, 1906274.
- [69] B. J. Boyd, A. Galle, M. Daglas, J. V. Rosenfeld, R. Medcalf, *J. Drug Targeting* **2015**, *23*, 847.